

AEDC-TR-76-67
AFRPL-TR-76-38

DOC_NUM SER CN
UNC22519-PDC A 1



**CONDENSATION SCALING LAWS FOR RESERVOIR AND NOZZLE
PARAMETERS AND GAS SPECIES AS DETERMINED BY
LASER SCATTERING EXPERIMENTS**

**VON KÁRMÁN GAS DYNAMICS FACILITY
ARNOLD ENGINEERING DEVELOPMENT CENTER
AIR FORCE SYSTEMS COMMAND
ARNOLD AIR FORCE STATION, TENNESSEE 37389**

September 1976

Interim Report for Period 1 July 1974 — 30 June 1975

Approved for public release; distribution unlimited.

Prepared for

**AIR FORCE ROCKET PROPULSION LABORATORY (DYSP)
EDWARDS AIR FORCE BASE, CALIFORNIA 93523**

NOTICES

When U. S. Government drawings specifications, or other data are used for any purpose other than a definitely related Government procurement operation, the Government thereby incurs no responsibility nor any obligation whatsoever, and the fact that the Government may have formulated, furnished, or in any way supplied the said drawings, specifications, or other data, is not to be regarded by implication or otherwise, or in any manner licensing the holder or any other person or corporation, or conveying any rights or permission to manufacture, use, or sell any patented invention that may in any way be related thereto.

Qualified users may obtain copies of this report from the Defense Documentation Center.

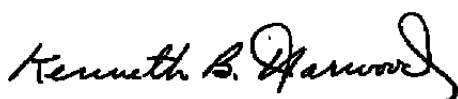
References to named commercial products in this report are not to be considered in any sense as an endorsement of the product by the United States Air Force or the Government.

This report has been reviewed by the Information Office (OI) and is releasable to the National Technical Information Service (NTIS). At NTIS, it will be available to the general public, including foreign nations.

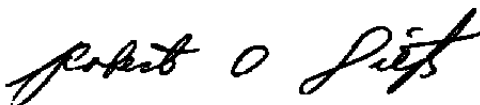
APPROVAL STATEMENT

This technical report has been reviewed and is approved for publication.

FOR THE COMMANDER



KENNETH B. HARWOOD
Major, CF
Research & Development
Division
Directorate of Technology



ROBERT O. DIETZ
Director of Technology

UNCLASSIFIED

REPORT DOCUMENTATION PAGE		READ INSTRUCTIONS BEFORE COMPLETING FORM
1 REPORT NUMBER AEDC-TR-76-67 AFRPL-TR-76-38	2 GOVT ACCESSION NO.	3 RECIPIENT'S CATALOG NUMBER
4 TITLE (and Subtitle) CONDENSATION SCALING LAWS FOR RESERVOIR AND NOZZLE PARAMETERS AND GAS SPECIES AS DETERMINED BY LASER SCATTERING EXPERIMENTS		5 TYPE OF REPORT & PERIOD COVERED Interim Report, 1 July 1974 - 30 June 1975
7 AUTHOR(s) W. D. Williams and J. W. L. Lewis, ARO, Inc.		6. PERFORMING ORG. REPORT NUMBER
9 PERFORMING ORGANIZATION NAME AND ADDRESS Arnold Engineering Development Center (DY) Air Force Systems Command Arnold Air Force Station, TN 37389		8 CONTRACT OR GRANT NUMBER(s)
11 CONTROLLING OFFICE NAME AND ADDRESS Arnold Engineering Development Center (DYFS) Arnold Air Force Station, TN 37389		10. PROGRAM ELEMENT PROJECT, TASK AREA & WORK UNIT NUMBERS Program Elements 62302F 65807F
14 MONITORING AGENCY NAME & ADDRESS (if different from Controlling Office)		12. REPORT DATE September 1976
		13 NUMBER OF PAGES 44
		15 SECURITY CLASS. (of this report) UNCLASSIFIED
		15a DECLASSIFICATION/DOWNGRADING SCHEDULE N/A
16 DISTRIBUTION STATEMENT (of this Report) Approved for public release; distribution unlimited.		
17 DISTRIBUTION STATEMENT (of the abstract entered in Block 20, if different from Report)		
18 SUPPLEMENTARY NOTES Available in DDC.		
19 KEY WORDS (Continue on reverse side if necessary and identify by block number) condensation Rayleigh scattering expansion flow fields laser beams		
20 ABSTRACT (Continue on reverse side if necessary and identify by block number) A study of the condensation of gases in expansion flow fields has been performed using laser Rayleigh scattering with the goal of determining the dependence of the spatial location of onset and subsequent condensate growth with gas reservoir conditions, gas source parameters, and gaseous species. Sonic orifice and conical nozzle expansions of N ₂ were studied for the range of reservoir pressure (P ₀) values from 0.26 to 10.2 atm at a nominal reservoir		

UNCLASSIFIED

UNCLASSIFIED

20. ABSTRACT (Continued)

temperature (T_0) of 285K. The conical nozzle expansions included the nozzle half angles ($\theta_{1/2}$) of 5.60, 9.0, and 14.5 deg. Finally, sonic orifice expansions produced by sources of two different diameters (D) were investigated for flow fields of Ar, N₂, O₂, and CO. The Rayleigh scattered intensity for the sonic orifice expansions was found to vary as $P_0^2 D$ during the initial phase of condensation onset and to vary as $P_0^3 D^2$ in the spatial regions of the flow field for which massive condensation existed. The massive condensation region of the nozzle expansions yielded scattered intensities which varied as $P_0^3 D \tan \theta_{1/2}$. The spatial location of massive condensation onset scaled as $(P_0^2 D)^{-1/4}$ for the sonic orifices and as $(P_0^2 D \cot \theta_{1/2})^{-1/4}$ for the conical nozzles. Through the use of reduced values of P_0 , D , and T_0 , nondimensionalized by appropriate intermolecular potential parameters, similar gases were found to have a common onset of condensation locus in a reduced pressure-temperature domain.

PREFACE

The work reported herein was conducted by the Arnold Engineering Development Center (AEDC), Air Force Systems Command (AFSC), at the request of the Air Force Rocket Propulsion Laboratory (AFRPL/DYSP), under Program Elements 62302F and 65807F. The AFRPL project monitor was Lieutenant I. Lee Witbracht. The results of the research were obtained by ARO, Inc. (a subsidiary of Sverdrup & Parcel and Associates, Inc.), contract operator of AEDC, AFSC, Arnold Air Force Station, Tennessee, under ARO Project Numbers V32S-11A, V32S-37A, and V32S-51A. The authors of this report were W. D. Williams and J. W. L. Lewis, ARO, Inc. The manuscript (ARO Control No. ARO-VKF-TR-76-16) was submitted for publication on February 11, 1976.

The authors wish to express their appreciation to M. Kinslow, ARO, Inc., for development of the condensation calculation discussed in Section 4.4.

CONTENTS

	<u>Page</u>
1.0 INTRODUCTION	7
2.0 RAYLEIGH SCATTERING	8
3.0 EXPERIMENTAL APPARATUS	9
4.0 RESULTS AND ANALYSIS	
4.1 Rayleigh Scattering Results	12
4.2 Analysis of Scaling	23
4.3 Correlation of Temperature, Rayleigh Scattering, and Depolarization Ratio Measurements with Condensation	31
4.4 Comparison of Condensation Calculations with Measurements	36
5.0 DISCUSSION AND SUMMARY	37
REFERENCES	39

ILLUSTRATIONS

Figure

1. Experimental Arrangement	10
2. Sonic Orifice and Conical Nozzle Schematics	11
3. Axial Variation of I' (II) for All N_2 Reservoir Pressures and Sonic Orifice Diameters Investigated	13
4. Axial Variation of I' (II) for All CO Reservoir Pressures Investigated	13
5. Axial Variation of I' (II) for All O_2 Reservoir Pressures Investigated	14
6. Axial Variation of I' (II) for All Ar Reservoir Pressures Investigated	14
7. Axial Variation of I' (II) for All N_2 Reservoir Pressures Investigated, $\theta_{1/2} = 5.63$ deg	15
8. Axial Variation of I' (II) for All N_2 Reservoir Pressures Investigated, $\theta_{1/2} = 9.0$ deg	15
9. Axial Variation of I' (II) for All N_2 Reservoir Pressures Investigated, $\theta_{1/2} = 14.5$ deg	16

<u>Figure</u>	<u>Page</u>
10. Radial Variation of I' (II) for an N_2 Reservoir Pressure of 10.2 atm at Three Axial Positions, $\theta_{1/2} = 14.5$ deg.	16
11. Flow Visualization Photograph, Axial Scan, N_2 , $P_O = 10.2$ atm, $\theta_{1/2} = 14.5$ deg	17
12. Axial Variation of Scattering Function, f , for 14.5-deg Nozzle, N_2 Gas	18
13. Axial Variation of Scattering Function, f , for Sonic Orifice, $D = 1.325$ mm, N_2 Gas	19
14. Diagram of Expansion Process	20
15. Variation of \hat{x}_θ/\hat{x}_s , Degrees of Supercooling, and Supersaturation Ratio with Reservoir Pressure for the Three Conical Nozzles Investigated	21
16. Variation of \hat{x}_θ/\hat{x}_s with Reservoir Pressure for Sonic Orifices	21
17. Supersaturation Ratio versus Reservoir Pressure for Sonic Orifices	22
18. Degrees of Supercooling versus Reservoir Pressure for Sonic Orifices	22
19. Scaling of Conical Nozzle Condensation Onset	27
20. Scaling of Sonic Orifice Condensation Onset	27
21. Scattering Function Scaling	28
22. Condensation Onset Locus Using Reduced Values	28
23. Condensation Onset Locus Using Reduced Values	29
24. Axial Variation of I' (II), Number Density, Temperature, Mass Fraction (g), and Depolarization Ratio: 14.5-deg Conical Nozzle, $P_O = 10.2$ atm, N_2	31
25. Axial Variation of I' (II), Number Density, Temperature, and Mass Fraction: 14.5-deg Conical Nozzle, $P_O = 6.80$ atm, N_2	32
26. Axial Variation of I' (II), Number Density, Temperature, and Mass Fraction: 14.5-deg Conical Nozzle, $P_O = 3.40$ atm, N_2	33

<u>Figure</u>	<u>Page</u>
27. Axial Variation of I^* (II) and Temperature: Sonic Orifice, $D = 1.325$ mm, $P_O = 7.44$ atm, N_2	33
28. Axial Variation of I^* (II) and Temperature: Sonic Orifice, $D = 1.325$ mm, $P_O = 5.59$ atm, N_2	34
29. Axial Variation of I^* (II) and Temperature: Sonic Orifice, $D = 1.325$ mm, $P_O = 3.72$ atm, N_2	34
30. Axial Variation of I^* (II) and Temperature: Sonic Orifice, $D = 1.325$ mm, $P_O = 2.79$ atm, N_2	35
31. Classical Nucleation Rates for Three N_2 Expansions, 14.5-deg Conical Nozzle	39

TABLES

1. Saturation and Condensation Onset Parameters for Gases and Sources Studied	23
2. Sonic Orifice Scaling Constants	24
3. Conical Nozzle Scaling Constants	25
4. Intermolecular Potential Constants	26
NOMENCLATURE	43

1.0 INTRODUCTION

Increased interest in the study of the fluid mechanics and rate kinetics of condensation processes in expansion flow fields has resulted from a heightened desire both to prevent their occurrence, such as in aerodynamic simulation facilities, and to exploit them for such applications as molecular beam studies and the possible use of the injection of charged clusters for refueling of fusion devices. Many investigations (Refs. 1 through 3) have used mass spectrometric-type sampling diagnostics which are necessarily located in the far-field, low density region of the expansion and, consequently, distant from the spatial region of condensation onset and growth. Therefore, such measurements observe the results of the integrated rate kinetic processes along the sampled streamtube. It is obviously desirable to obtain nonperturbing, spatially resolved measurements in the vicinity of the growth processes to obviate the need for inferral of information from downstream, far-field data, and optical scattering techniques offer such a possible diagnostic approach.

Although light scattering was used as early as 1951 (Ref. 4) to study condensation in expansion flows, the technique did not exhibit its power until the early, inadequate light sources were replaced by laser sources. The most notable application of laser scattering to such condensation studies includes that of Wegener and his students, who emphasized investigations of the condensation of an impurity species in a non-condensing gas, i. e., the isothermal condensation process (Refs. 5 through 7). Further, Beylich (Refs. 8 and 9) has applied this technique to the study of CO₂ condensation, and Daum and his associates (Ref. 10) have studied the condensation of air expansions.

In these referenced works where appropriate data were available, the condensate radii ranged in value from 10 to approximately 100 Å with number densities from 10^{11} to 10^{14} cm⁻³, indicating that the scattering is adequately described by the Rayleigh theory rather than the more complicated Mie formulation. With these results used as a basis, laser Rayleigh scattering diagnostics have been used at AEDC to study a variety of condensing flows (Refs. 11 through 14). Further, Raman scattering (Refs. 13 through 16) has been used for the measurement of both monomer density and temperature throughout the flow field, including the region of the onset of condensation. The purpose of the experiments reported herein was to use laser Rayleigh scattering as a diagnostic to locate the axial onset of condensation in an

expansion flow field and measure the spatial growth characteristics of the condensed clusters. With systematic variation of gas species, reservoir pressure, orifice or throat diameter, and nozzle expansion angle, these measurements provided determination of the methods of scaling condensation phenomena with gas species and source reservoir conditions and geometry.

2.0 RAYLEIGH SCATTERING

Since the basic equations and rationale for the application of Rayleigh scattering to the study of condensing gas flow fields is presented in Refs. 11 through 14, only a brief summary is given.

For an incident laser beam of wavelength λ and intensity I_0 focused within a gas sample of number density N with species polarizability α , the scattered intensity, I , which is normalized by I_0 , is given by

$$I = K_\alpha N \alpha^2 / \lambda^4 \quad (1)$$

where the constant K_α collects all unimportant transmission and calibration factors. For a scatterer of radius "a" which is characterized by bulk properties, it is known that $\alpha \propto a^3$, which indicates the sensitivity of the process to scatterer size. If one assumes the condensing flow field to be composed of a collection of gas phase monomers and molecular clusters, or i-mers, where i is the number of molecules per cluster, the single Rayleigh scattering intensity with polarization parallel to the incident beam's plane of polarization is (Ref. 11)

$$I'(\text{II}) = \sum_{i=1} \left(\frac{N_i}{N_0} \right) \left(\frac{\alpha_i}{\alpha_1} \right)^2 \quad (2)$$

where N_0 is the reservoir number density. The scattered intensity $I'(\text{II})$ includes the further normalization provided by the scattered intensity from a collection of monomers of number density N_0 .

For an uncondensed, isentropic expansion,

$$I'(\text{II}) = \left(\frac{N_1}{N_0} \right)^0 = I^0(\text{II}) \quad (3)$$

Super- and subscript zeros denote isentropic and reservoir conditions, respectively. The axial variation of $I^0(II)$ is provided by the method-of-characteristics solution (MOCS) (Ref. 17) for nozzle flow and by the Sherman-Ashkenas theory (Ref. 18) for sonic orifice flow.

Deviation of the measured I' (II) from $I^0(II)$ indicates the existence of condensation. A direct measure of the existence of clusters within the flow is given by the scattering function, f , which is written as

$$f = \left(\frac{I'(II)}{I^0(II)} \right) - 1 \approx \sum_{i=2} X_i \left(\frac{a_i}{a_1} \right)^2 \quad (4)$$

where X_i is the i -mer mole fraction. The approximation results because for small values of condensate mass fraction it is assumed that $N_1 \approx N_1^0 \approx N_T$, where N_T is the total local number density. Although the scattering function (f) is an ambiguous measure of the simultaneous increase in the mean cluster size and condensate mole fraction, the axial variation of f as a function of P_0 , D or D_t , $\theta_{1/2}$, and gas species yields empirical condensation scaling laws.

Assuming small clusters to be characterized by weak chemical bonding, the cluster polarizability is assumed to be additive; i. e., $\alpha_i = i\alpha_1$. Consequently, for a monodisperse distribution in cluster sizes, $i = J$ and $\alpha_J \approx J\alpha_1$, so that f is $J^2 X_J$. The condensate mass fraction, g , is

$$g = JX_J / [1 + (J - 1)X_J] \quad (5)$$

The depolarization ratio, ρ , of the mixture of monomers and J -mers is the ratio of the measured scattered intensity components polarized perpendicular and parallel to the incident plane of polarization; that is,

$$\rho = I'(I)/I'(II) \quad (6)$$

3.0 EXPERIMENTAL APPARATUS

Figure 1 shows the experimental configuration. A cylindrical vacuum chamber approximately 1.2 m in diameter and 3.0 m in length

which was equipped with LN_2 and 20K gaseous He pumping to provide a low pressure, 10^{-7} to 10^{-3} torr background environment for the vacuum flow-field expansion studies. The flow generators were mounted on a motor-driven, three-dimensional movement mechanism with an accuracy and reproducibility of 0.013 cm. The sonic orifices were of 1.325-, 3.2-, and 3.05-mm diameter with a diameter-to-thickness ratio greater than 20. The conical nozzles had a nominal throat diameter and nozzle length of 1.0 mm and 5.334 mm, respectively; the three nozzle half-angles were 14.5, 9.0, and 5.63 deg. Schematics of the sonic orifice and conical nozzle are shown in Fig. 2.

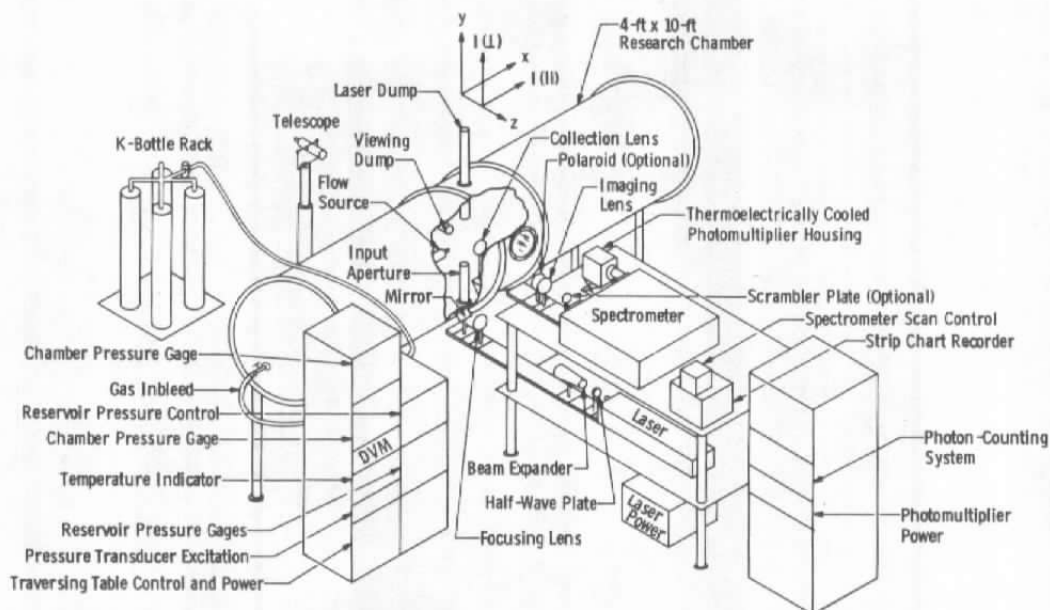


Figure 1. Experimental arrangement.

The gas reservoir was instrumented with standard, calibrated pressure and temperature gages. Gases were supplied from high pressure bottles, and the stated purity of the gases used was as follows: N_2 , 99.998 percent; O_2 , 99.5 percent; CO , 99.5 percent; Ar , 99.99 percent. No further purification was performed; to minimize effects of particulate matter, two 25.0-nm filters were installed in the inlet line.

As shown in Fig. 1, the flow is in the x-direction, the laser beam injection is along the y-axis, and scattered radiation is observed in the z-direction. For the Rayleigh scattering measurement the argon ion laser was operated at 1.0 W power at 514.5 nm;

however, for flow visualization 4.0 W total laser output power was used. The incident laser radiation polarization was rotated along the x-direction, expanded, and focused onto the chamber centerline. Light scattered from the focal volume was collected by an $f/2$ lens system, collimated, and focused onto the input slit of a 0.85-m double grating spectrometer. For the Rayleigh scattering measurements, HN-22 Polaroid® material was placed in the collimated light path, and a polarization scrambler was placed immediately in front of the spectrometer entrance slit. The entrance slit aperture setting, collection optics magnification, and beam focusing together resulted in observation of a 1.5-mm-long, 50- to 100- μ m-diam cylindrical scattering volume.

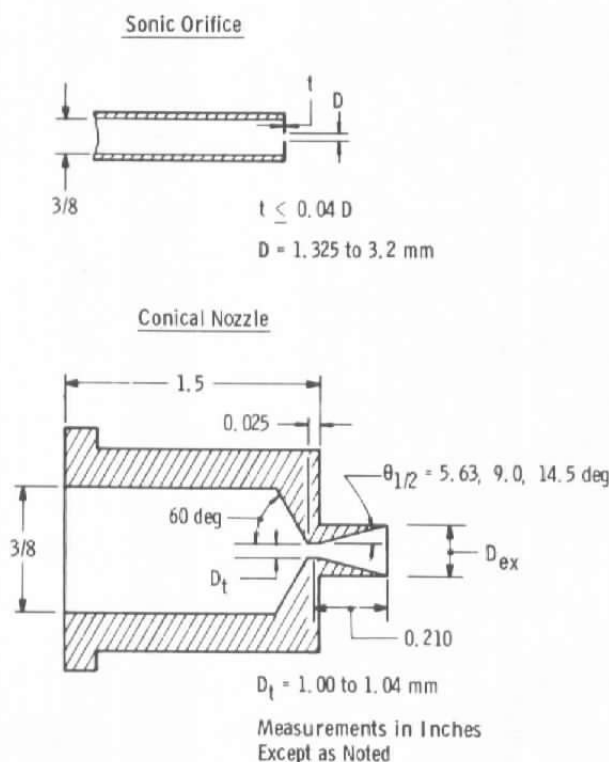


Figure 2. Sonic orifice and conical nozzle schematics.

The detector was a thermoelectrically cooled EMI-9502B photomultiplier, and the output was processed by an Ortec® photon-counting system for either digital display or strip chart recording.

Several laser beam input apertures were used to reduce background radiation resulting from laser plasma light and forward

scatter off of optical components. Laser and viewing dumps were provided for further reduction of background signals, and all optically accessible surfaces were either painted with a flat black coating or covered with a black flocking material.

4.0 RESULTS AND ANALYSIS

4.1 RAYLEIGH SCATTERING RESULTS

Figures 3 through 6 show the experimental results of the axial profiles of I' (II) for the N_2 , CO , O_2 , and Ar expansions from sonic orifices. Figures 7 through 9 show the axial variation of I' (II) for N_2 expansions from the three conical nozzles used. Theoretical predictions as obtained from the Sherman-Ashkenas theory or the MOCS are also shown. It is observed that the onset of condensation is manifested by a dramatic increase of I' (II) relative to the isentropic prediction. The onset of condensation moves nearer the saturation point as P_0 increases, and, with the exception of the region of discontinuity in the MOCS nozzle calculations, I' (II) is in good agreement with the calculated values prior to condensation onset. Furthermore, it can be seen that for the lowest P_0 values the metastable gas sample supports a supersaturated state for approximately 30 throat or sonic orifice diameters before condensing. It is also noted that the massive condensate growth for the nozzle flows is quite abrupt, whereas the massive condensate growth region for the sonic orifice flow is generally preceded by a gradual deviation from the isentropic prediction.

Radial profiles of I' (II) are shown in Fig. 10 for the $P_0 = 10.2$ atm, $\theta_{1/2} = 14.5$ -deg conical nozzle for three values of \hat{x} . The data for $\hat{x} = 17.35$ are interesting in that two scattering peaks are symmetrically located off the centerline. Similar observations have been reported by Beylich (Ref. 8) in a study of CO_2 condensation in a nozzle flow. From Fig. 9 it is seen that at $\hat{x} = 17.35$, condensation has not begun on the axial centerline. However, Fig. 10 shows that onset has already begun for $r/D_t > 0$. Figure 11 shows photographic observation of the $P_0 = 10.2$ atm, $\theta_{1/2} = 14.5$ -deg nozzle flow field, and the nozzle, the dark isentropic expansion zone, and the bright onset zone are clearly evident, as is filamentary structure with the condensation growth region.

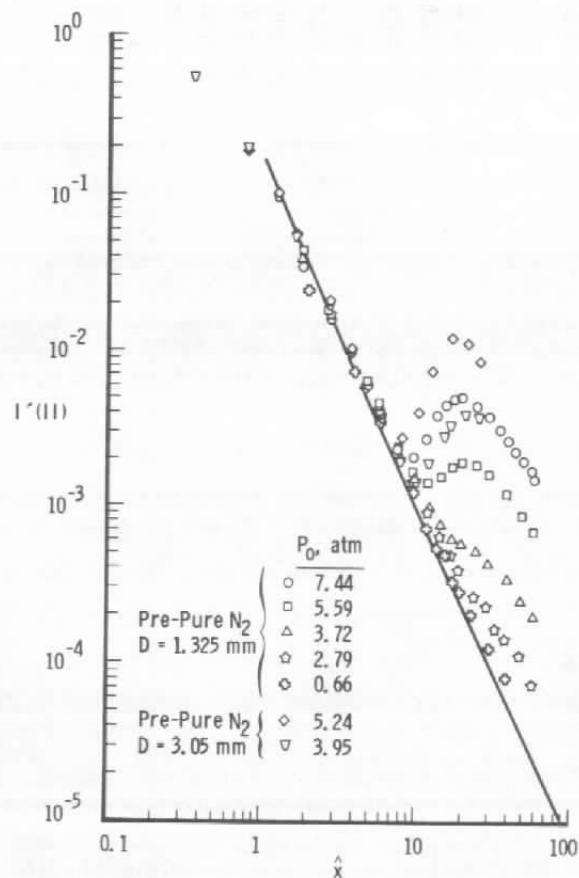


Figure 3. Axial variation of $I'(II)$ for all N_2 reservoir pressures and sonic orifice diameters investigated.

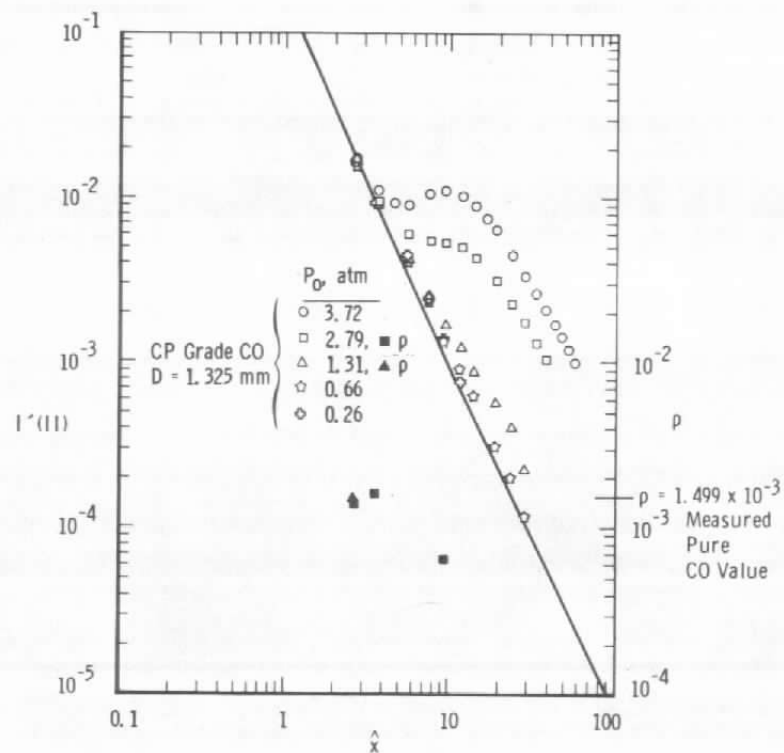


Figure 4. Axial variation of $I'(II)$ for all CO reservoir pressures investigated.

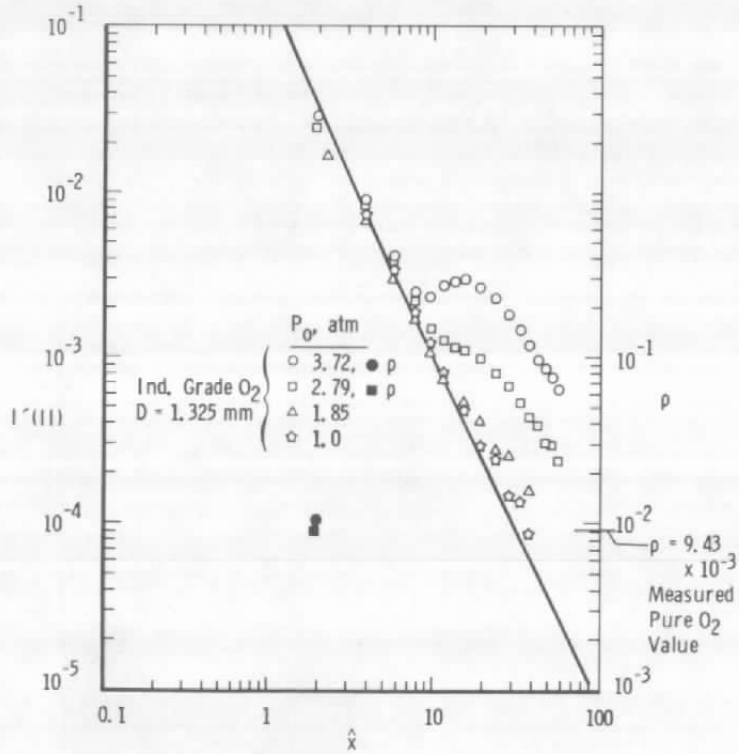


Figure 5. Axial variation of $I'(II)$ for all O_2 reservoir pressures investigated.

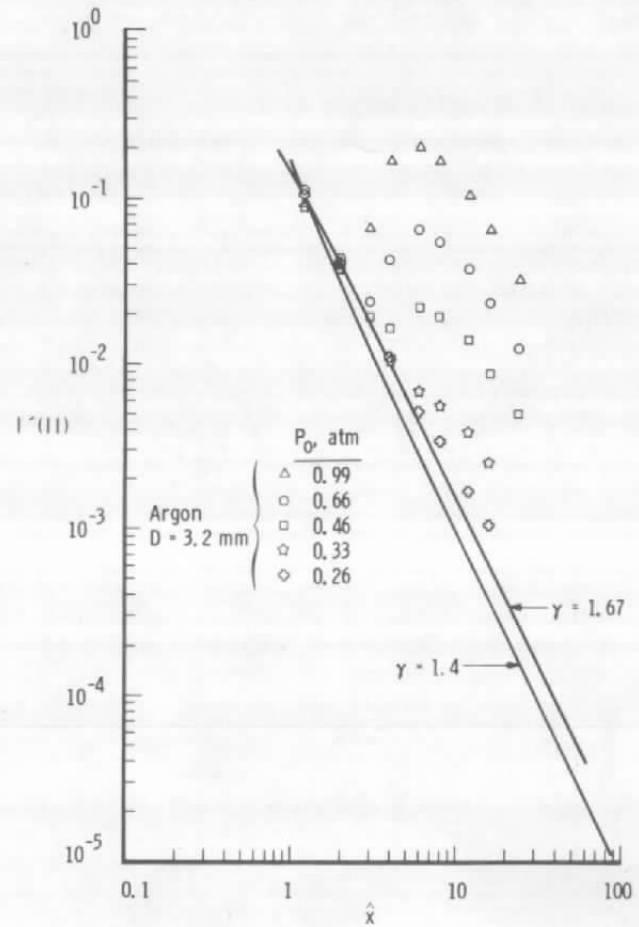


Figure 6. Axial variation of $I'(II)$ for all Ar reservoir pressures investigated.

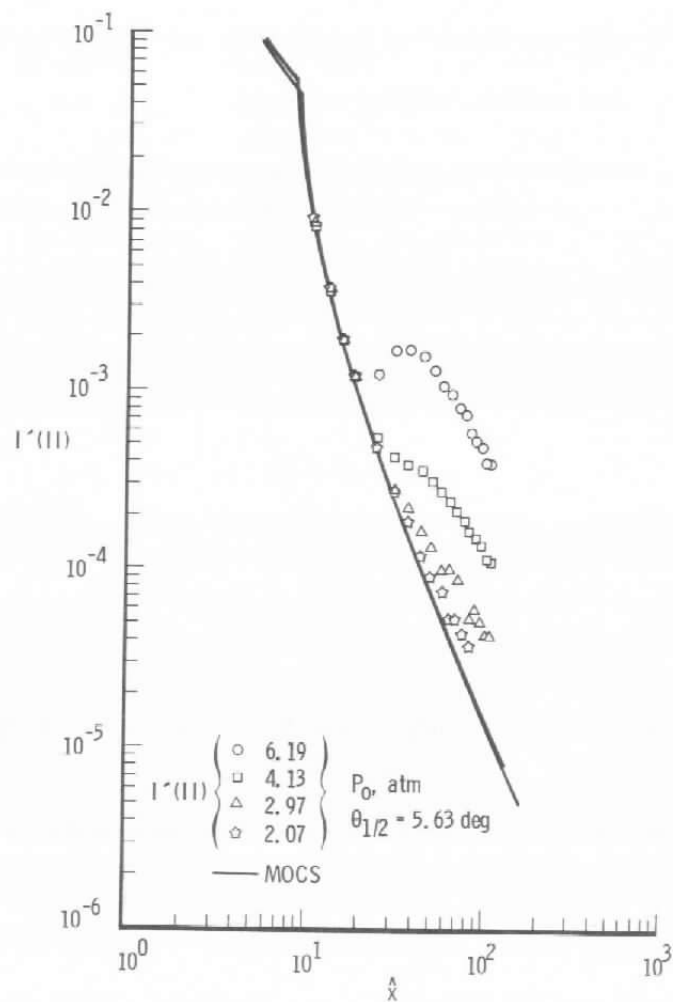


Figure 7. Axial variation of $I'(II)$ for all N_2 reservoir pressures investigated, $\theta_{1/2} = 5.63$ deg.

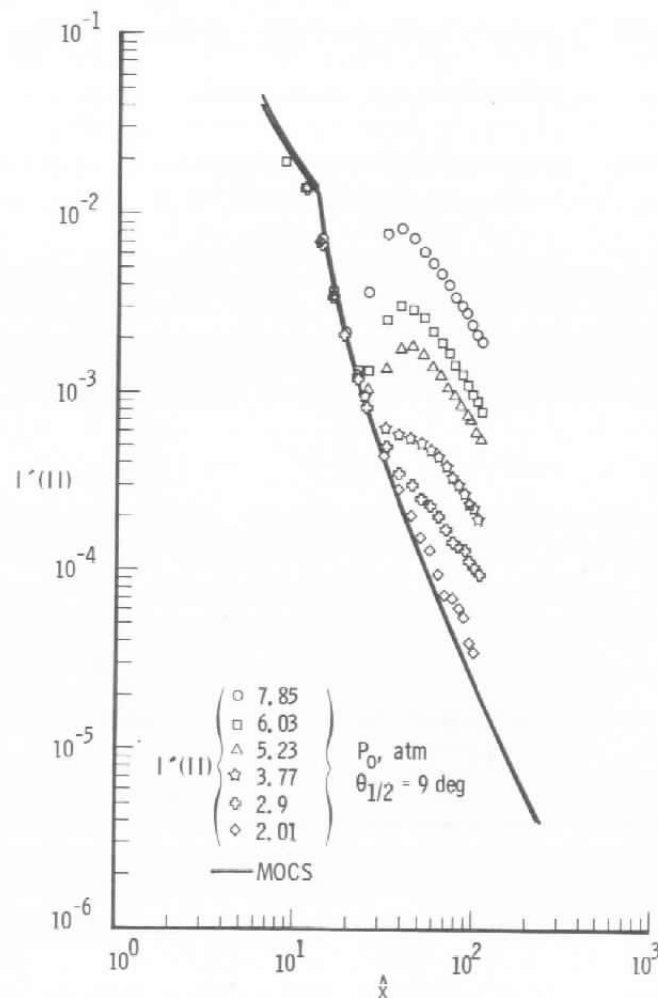


Figure 8. Axial variation of $I'(II)$ for all N_2 reservoir pressures investigated, $\theta_{1/2} = 9.0$ deg.

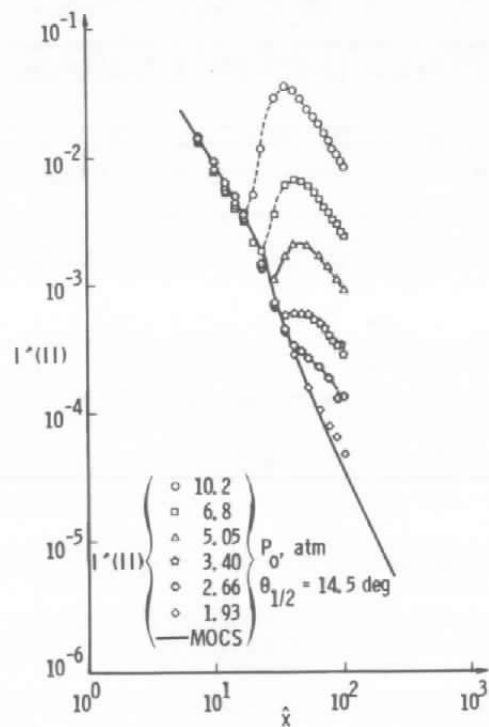


Figure 9. Axial variation of $I'(II)$ for all N_2 reservoir pressures investigated, $\theta_{1/2} = 14.5$ deg.

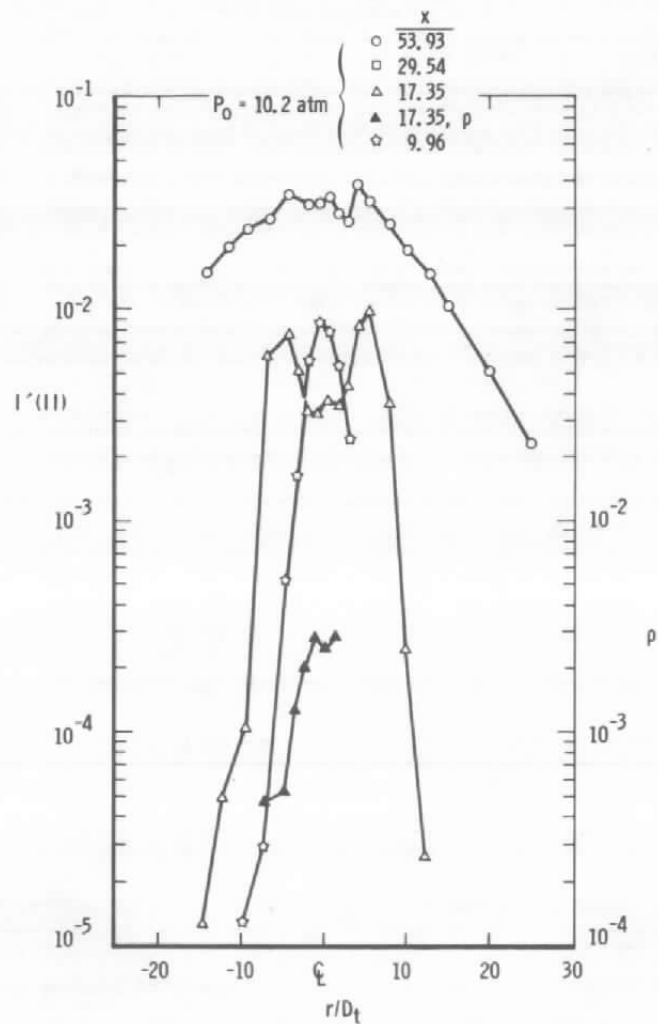


Figure 10. Radial variation of $I'(II)$ for an N_2 reservoir pressure of 10.2 atm at three axial positions, $\theta_{1/2} = 14.5$ deg.

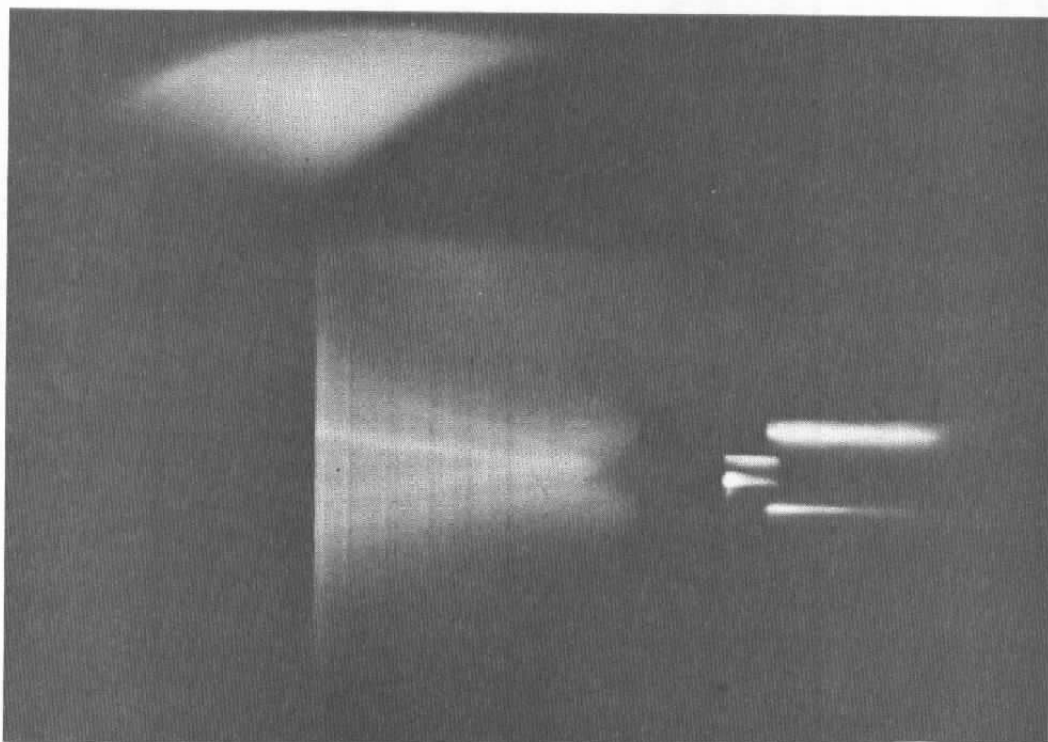


Figure 11. Flow visualization photograph, axial scan,
 N_2 , $P_0 = 10.2$ atm, $\theta_{1/2} = 14.5$ deg.

Figures 12 and 13 show the axial variation of the scattering function, f , with N_2 gas for the 14.5-deg half-angle nozzle and the $D = 1.325$ -mm sonic orifice, respectively. These plots are typical of all the f versus \hat{x} plots obtained. It is noted that in these semi-logarithmic plots the f values for a given P_0 and nozzle (or orifice) form straight lines, and it is the intersection of these straight lines with the \hat{x} -axis that is used to determine the onset of condensate growth. These axial onset locations are denoted by \hat{x}_θ . The rapid increase in f following onset is obvious, as are the orders of magnitude increase in f as the reservoir pressure increases.

Using the vapor pressure data of Hilsenrath, et al. (Ref. 19) and the isentropic solution for each particular flow field investigated, the saturation values of pressure and temperature, P_s and T_s , respectively, are obtained, as are similar values at condensation onset, denoted by P_θ and T_θ . The isentropic supersaturation pressure ratio, $(s_\theta)^0$, is defined as

$$(s_\theta)^0 \equiv P_s/P_\theta \quad (7)$$

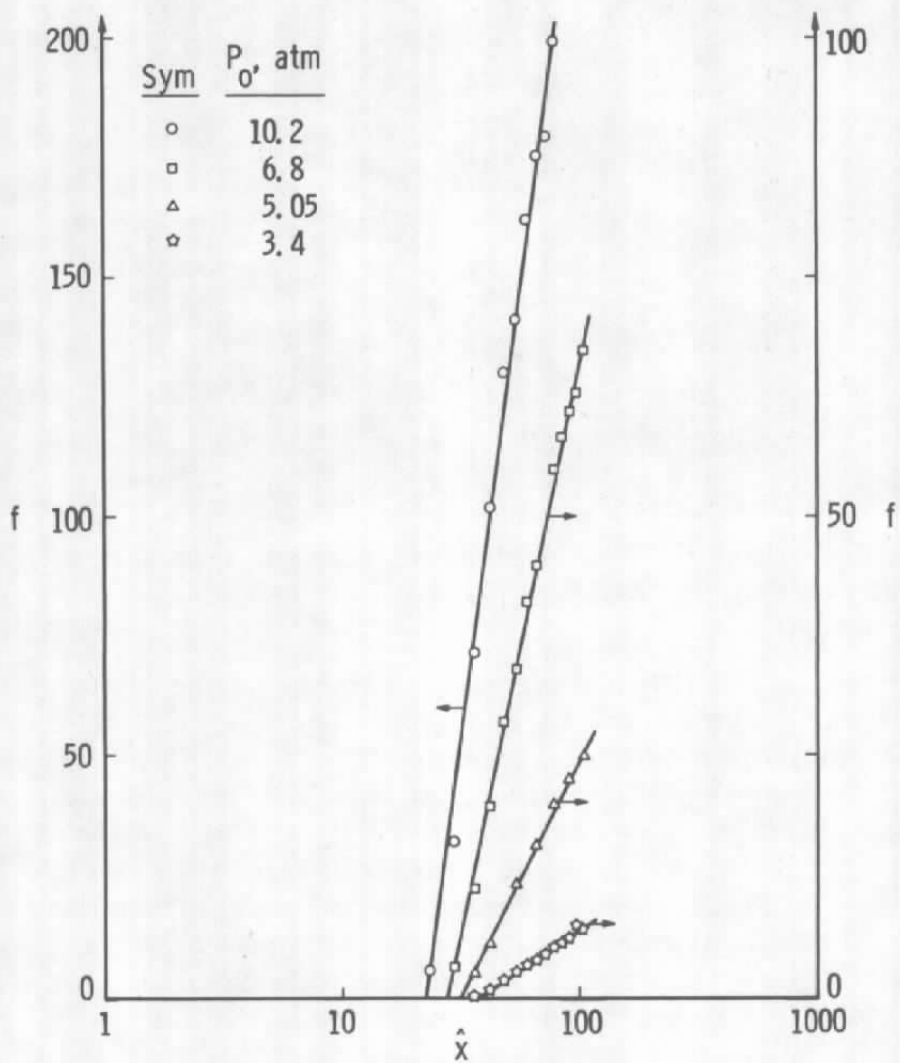


Figure 12. Axial variation of scattering function, f , for 14.5-deg nozzle, N_2 gas.

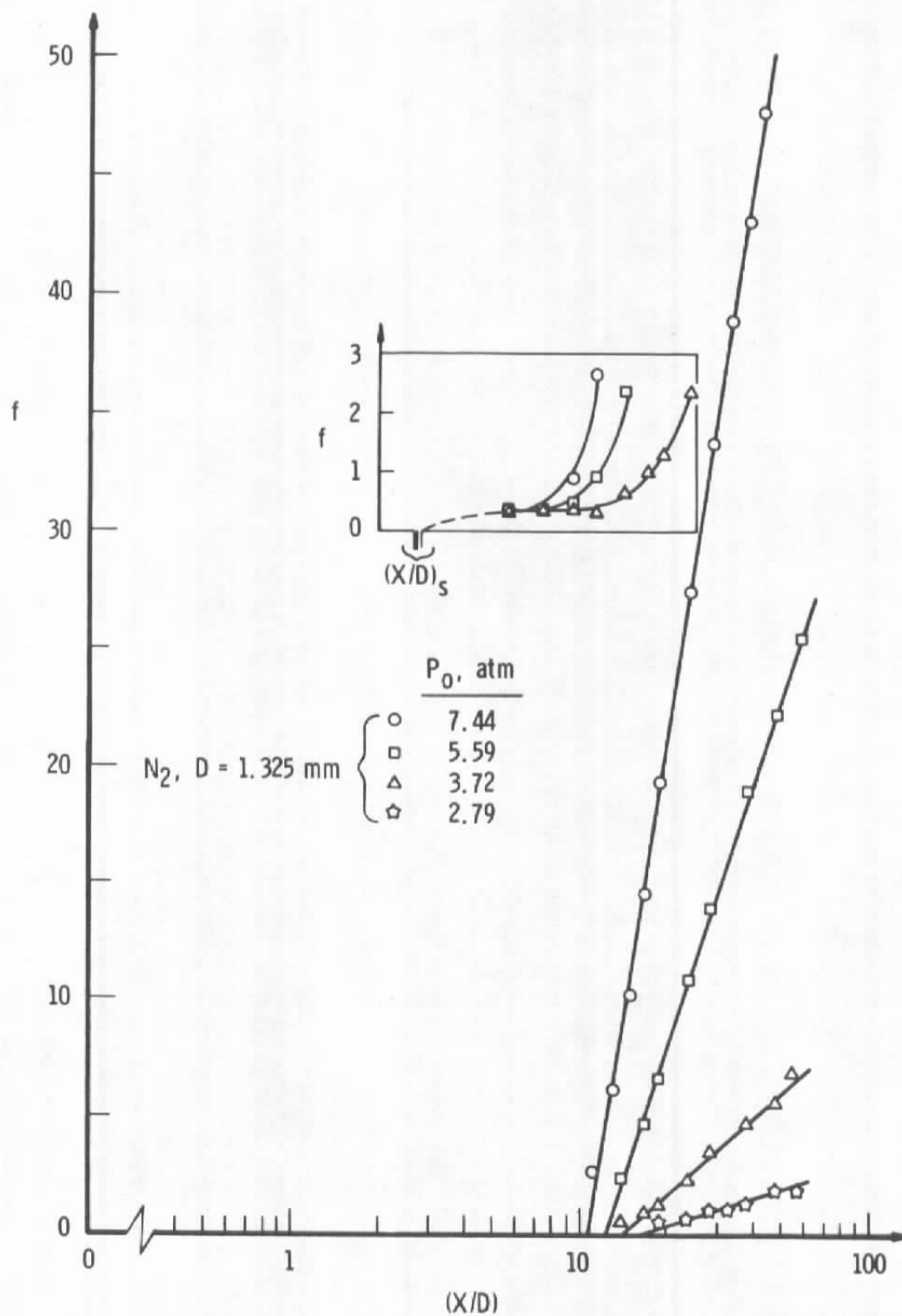


Figure 13. Axial variation of scattering function, f , for sonic orifice, $D = 1.325$ mm, N_2 gas.

and the isentropic degrees of supercooling, $(s'_\theta)^0$, are defined as

$$(s'_\theta)^0 \equiv T_s - T_\theta \quad (8)$$

It should be noted that the supersaturation ratio defined here is not the normal definition of the ratio of the pressure at onset to the equilibrium vapor pressure at onset, $P_\theta/P_{v\theta}$. The $(s_\theta)^0$ values are orders of magnitude lower than the normally defined supersaturation ratios for the flow fields investigated here. These supersaturation parameters are illustrated in Fig. 14, a diagram of the expansion process.

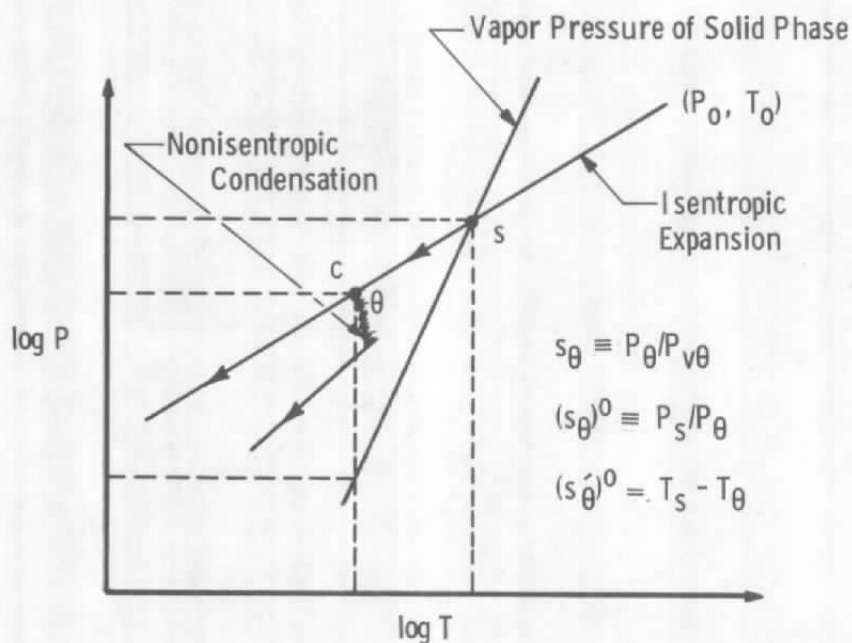


Figure 14. Diagram of expansion process.

Figure 15 shows the variation of \hat{x}_θ/\hat{x}_s , $(s_\theta)^0$, and $(s'_\theta)^0$ with P_0 for the three conical nozzles studied. The approach of the location of condensation onset toward the saturation point as P_0 increases is obvious. The highest value of supersaturation ratio for a given P_0 is achieved by the $\theta_{1/2} = 5.63$ -deg nozzle flow, and typically 40K supercooling is possible. Figures 16, 17, and 18 show the variation of \hat{x}_θ/\hat{x}_s , $(s_\theta)^0$, and $(s'_\theta)^0$ with P_0 for the sonic orifices studied. The highest value of supersaturation ratio for a given P_0 was achieved by the $D = 1.325$ -mm, N_2 expansion. Supercooling typically ranged from 30 to 50K. Table 1 is a tabulation of the saturation, condensation onset, and supersaturation parameters for the various gases and sources.

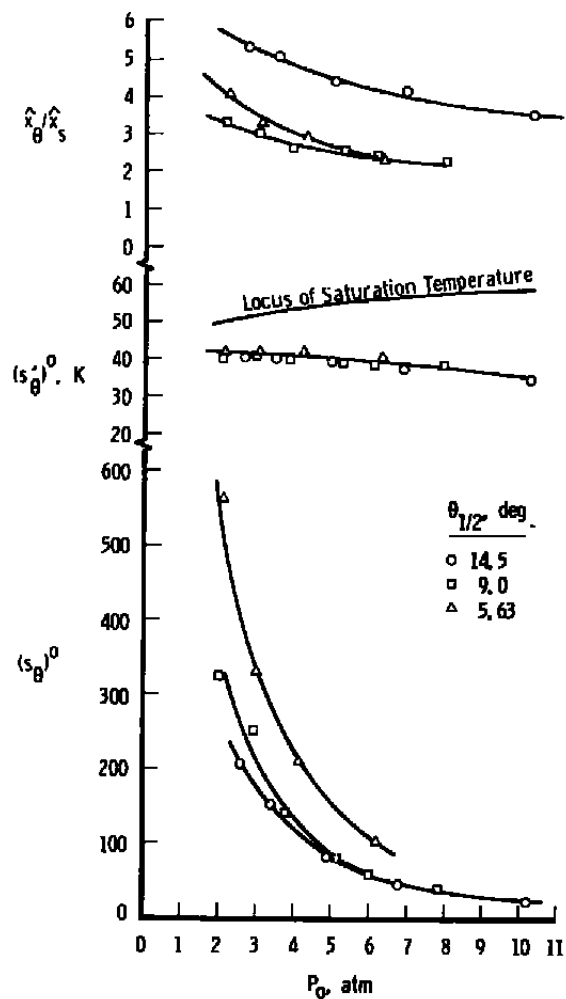


Figure 15. Variation of \hat{x}_θ/\hat{x}_s , degrees of supercooling, and supersaturation ratio with reservoir pressure for the three conical nozzles investigated.

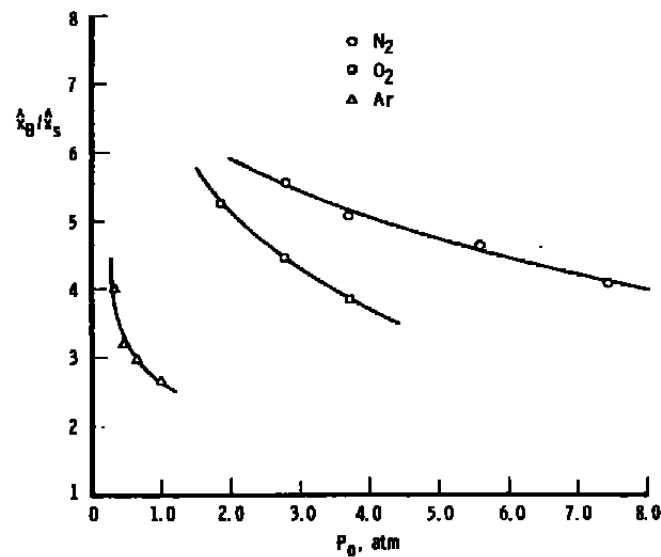


Figure 16. Variation of \hat{x}_θ/\hat{x}_s with reservoir pressure for sonic orifices.

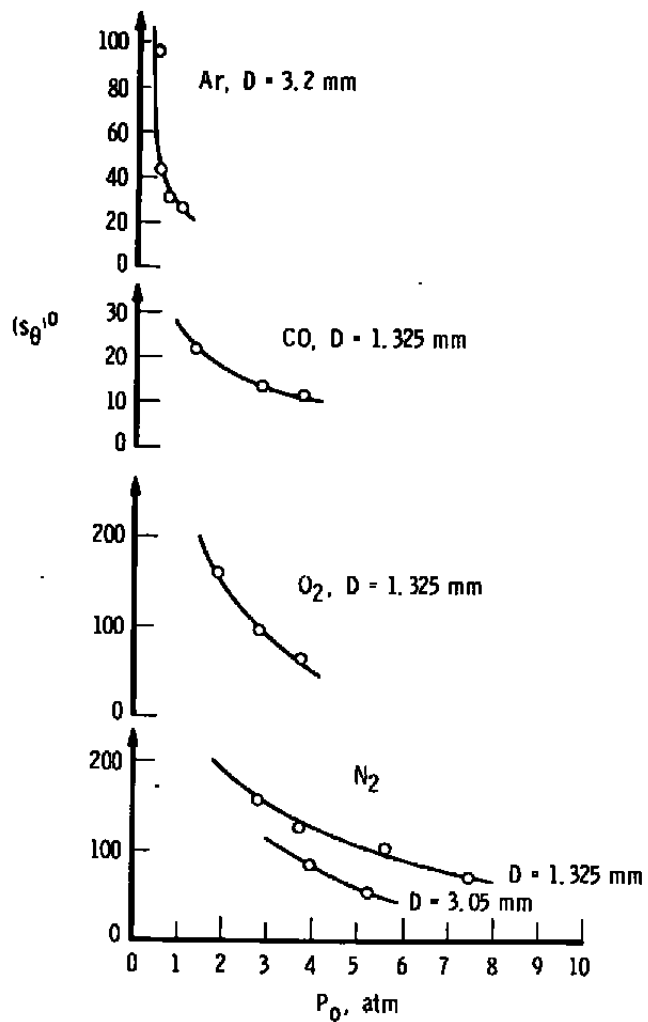


Figure 17. Supersaturation ratio versus reservoir pressure for sonic orifices.

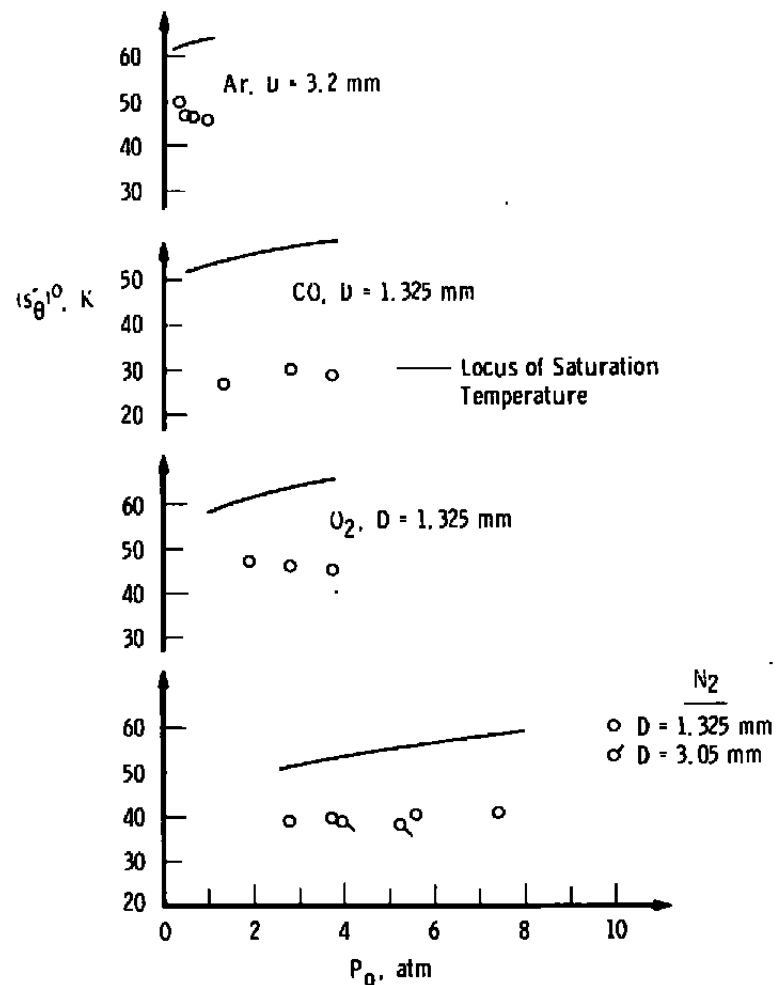


Figure 18. Degrees of supercooling versus reservoir pressure for sonic orifices.

**Table 1. Saturation and Condensation Onset Parameters
for Gases and Sources Studied**

Gas	$\theta_{1/2}$ (degrees)	Pinlet or Orifice Diam (mm)	T_0 (K)	P_0 (atm)	x_s	P_s (torr)	T_s (K)	x_θ	P_θ (torr)	T_θ (K)	$t_{s,0}$	$t_{s,\theta}$
N_2 ↓	14.5 ↓	1.04 ↓	288	19.2	5.3	27.1	58.5	22.4	1.19	23.9	22.7	34.6
			287	6.80	6.6	18.3	56.8	27.6	0.40	19.1	45.5	37.5
			286	5.05	7.1	11.3	54.8	31.5	0.138	15.4	81.9	39.4
			284	3.40	7.4	7.0	52.8	37.8	0.046	12.5	152.2	40.3
			285	2.66	7.9	4.85	51.0	42.0	0.0235	11.2	206	40.1
			285	1.93	8.3	3.1	49.4					
N_2 ↓	9.0 ↓	1.00 ↓	285	7.85	9.8	22.5	57.5	22.6	0.459	18.8	49.1	38.7
			283	6.05	10.1	15.5	56.0	24.8	0.275	17.4	56.7	38.6
			286	5.23	10.6	12.8	55.0	27.2	0.16	15.6	81.3	39.4
			287	3.77	12.0	8.0	53.0	31.4	0.0579	12.9	140	40.1
			283	2.4	12.2	5.6	51.5	37.3	0.0222	10.6	250	40.9
			281	2.01	12.4	3.4	49.5	41.3	0.0106	9.5	323	40.3
N_2 ↓	5.63 ↓	1.00 ↓	284	6.19	9.3	16.5	56.0	21.9	0.162	15.1	131.9	40.9
			286	4.13	9.4	9.4	54.0	27.7	0.045	11.7	239	42.3
			285	2.97	9.5	5.8	51.0	31.5	0.0176	9.9	329.5	42.1
			283	2.07	9.7	3.6	50.0	39.5	0.0064	8.0	563	42.0
N_2 ↓	N/A ↓	1.325 ↓	291	7.44	2.65	20.6	58.0	10.8	0.29	16.9	71.1	41.1
			292	5.59	2.7	12.9	55.5	12.5	0.125	14.9	103.3	40.6
			289	3.72	2.8	7.9	53.0	14.2	0.063	13.3	125.4	39.7
			290	2.79	2.95	4.9	51.0	16.4	0.0314	11.9	156	39.1
N_2 ↓	N/A ↓	3.05 ↓	285	5.24	2.6	14.6	56.4	9.64	0.274	18.2	53.3	38.2
			285	3.95	2.7	9.11	54.0	11.75	0.110	15.1	82.7	38.9
O_2 ↓	N/A ↓	1.325 ↓	283	3.72	2.24	16.6	65.0	8.65	0.256	19.9	64.8	45.2
			285	2.79	2.31	11.1	63.5	10.5	0.116	17.2	95.7	46.3
			283	1.85	2.38	8.18	61.4	12.5	0.051	14.4	160.5	47.0
			281	1.0	2.55	3.05	58.0					
CO ↓	N/A ↓	1.325 ↓	291	3.72	2.65	5.4	58.0	5.75	0.61	29.1	11.6	28.9
			284	2.79	2.6	7.7	57.5	5.96	0.57	27.5	13.5	32.0
			285	1.31	2.75	3.2	54.0	6.05	0.147	27.2	21.8	26.8
			283	0.66	2.9	1.38	52.0					
			283	0.26	3.1	0.46	49.0					
A^+ ↓	N/A ↓	3.23 ↓	280	0.987	1.18	19.5	63.3	3.14	0.84	18.2	23.2	45.8
			281	0.658	1.20	12.0	63.5	3.56	0.375	15.5	30.9	46.5
			277	0.461	1.22	8.0	62.6	3.88	0.176	13.6	43.9	46.4
			275	0.329	1.24	5.6	62.2	4.95	0.056	9.56	96.5	49.4
			276	0.263	1.25	4.25	62.4					

4.2 ANALYSIS OF SCALING

Empirical functional relations of f with \hat{x} , \hat{x}_θ , P_0 , and D or D_t were obtained using the results of the axial variation of the scattering function data. These axial variations were represented by the form

$$\hat{x} = \hat{x}_\theta e^{bf} \quad (9)$$

and by graphical determination it was found that " b " could be represented by

$$b = KP_0^{-n_0} \quad (10)$$

For the sonic orifices it was found that K could be represented by

$$K = c_0 D^{-c_1} \quad (11)$$

where c_0 , c_1 , and n_0 are constants. Further graphical results showed that

$$\hat{x}_\theta = c_2 D^{-c_3} P_o^{-n_1} \quad (12)$$

for the sonic orifices, where c_2 , c_3 , and n_1 are constants. Table 2 is a tabulation of the sonic orifice scaling constants determined where there was sufficient data. For the conical nozzles it was determined that

$$K = c'_0 \cot \theta_{1/2} D_t^{-c_1} \quad (13)$$

Table 2. Sonic Orifice Scaling Constants

Gas	D (mm)	n_0	n_1	c_1	c_3
N ₂	1.325	2.94	0.222	2.02	(0.25)
	3.05	2.93	0.696		
O ₂	1.325	2.98	0.513		
CO	1.325	2.87			
Ar	3.2	3.03	0.49		

It should be noted that the nozzle throat diameter variation was extremely small and was a result only of imprecision during nozzle fabrication. Therefore, the variation of K with D_t was mainly inferred from the sonic orifice results, and it remains to be experimentally verified. Again, graphical results showed that

$$\hat{x}_\theta = c'_2 (\cot \theta_{1/2} D_t)^{-c_3} P_o^{-n_1} \quad (14)$$

where the variation with D_t is again mainly inferred. Table 3 is a tabulation of the conical nozzle scaling constants.

Table 3. Conical Nozzle Scaling Constants

Gas	D_t (mm)	$\theta_{1/2}$ (deg)	n_0	n_1	c_1	c_3
N ₂	1.04	14.5	2.98	0.525	(2)	(0.25)
	1.00	9.0				
	1.00	5.63				

Values of $n_1 = 0.5$ and $c_3 = 0.25$ are used to show the scaling of condensation onset with P_0 , D , or D_t and $\theta_{1/2}$ in Figs. 19 and 20 for the conical nozzles and sonic orifices, respectively. It is seen that \hat{x}_θ for the conical nozzles is a linear function of $(P_0^2 D_t \cot \theta_{1/2})^{-1/4}$ and for the sonic orifices \hat{x}_θ is a linear function of $(P_0^2 D)^{-1/4}$.

Equations (9) through (14) may be used to write the scattering functions for the sonic orifices and conical nozzles as follows:

$$f = c_0^{-1} D^{c_1} P_0^{n_0} \ln \left[\frac{\hat{x} P_0^{n_1} D^{c_3}}{c_2} \right] = c_4 b^{-1} \ln [\hat{x} A] \quad (15)$$

and

$$f = (c_0')^{-1} D_t^{c_1} \tan \theta_{1/2} P_0^{n_0} \ln \left[\frac{\hat{x} P_0^{n_1} (D_t \cot \theta_{1/2})^{c_3}}{c_2'} \right] = c_4' b^{-1} \ln (\hat{x} A') \quad (16)$$

respectively. For values of $n_0 = 3$ and $c_1 = 2$ the scaling of the scattering function (or, in this case, of experimental values of b^{-1}) for the various gases and sources is shown in Fig. 21. It is noted that these choices of scaling constants give a good linear variation of the scattering function with the reservoir and gas source parameters used.

On the basis of far-field mass spectrometric sampling of sonic orifice jets of noble gases, it has been shown (Ref. 3) that the 12:6 Lennard-Jones potential parameters ϵ/k , ϵ/σ^3 , and σ are appropriate scaling parameters for the source temperature, pressure, and orifice diameter, respectively. It has been proposed (Ref. 20) that dimer

concentration for expanding jets scales as $P_O^2 D_{eq}$, and it has also been observed that light scattering in regions prior to massive condensate growth scales as $P_O^2 D$ (Ref. 12). Furthermore, the condensation onset locations, \hat{x}_θ , have been shown to be a function of $P_O^2 D_{eq}$ in this investigation. With this in mind the intermolecular potential constants (Ref. 21) given in Table 4 have been used to plot the condensation loci of the flow-fields studied in a reduced pressure-temperature plot. In Fig. 22, $P^*(D_{eq}^*)^{1/2}$ has been plotted versus T^* where

$$P^* = P_\theta / (\epsilon / \sigma^3), \quad (17)$$

$$T^* = T_\theta / (\epsilon / k), \quad (18)$$

and

$$D_{eq}^* = D / \sigma \quad (19)$$

for sonic orifices, while

$$D_{eq}^* = C(\gamma) D_t \cot \theta_{1/2} / \sigma \quad (20)$$

for conical nozzles.

Table 4. Intermolecular Potential Constants

Gas	$T^* = \epsilon/k$ (K)	ϵ (ergs)	$D^* = \sigma$ (cm)	$P^* = \epsilon/\sigma^3$ (torr)
N ₂	95.05	1.31×10^{-14}	3.70×10^{-8}	1.94×10^5
O ₂	117.5	1.62×10^{-14}	3.58×10^{-8}	2.65×10^5
CO	100.2	1.38×10^{-14}	3.76×10^{-8}	1.94×10^5
CO ₂	205	2.83×10^{-14}	4.07×10^{-8}	3.15×10^5
Ar	119.8	1.65×10^{-14}	3.40×10^{-8}	3.14×10^5

$C(\gamma = 1.4)$ is 0.86 (Ref. 22). It is noted in Fig. 22 that the homonuclear molecules N₂ and O₂ have a common condensation locus for the sonic orifice expansions, whereas monatomic Ar and polar CO

have widely different loci. The condensation loci for the nozzles are of identical slope but are displaced from each other. In Fig. 23, P^* has been plotted versus T^* for the homonuclear species studied. It is noted that the conical nozzle onset locus and the sonic orifice onset locus are very close to each other. The conical nozzle onset locus may be represented as follows:

$$P^* \propto T^{*5.1} \quad (21)$$

whereas for the sonic orifices,

$$P^* \propto T^{*5.9} \quad (22)$$

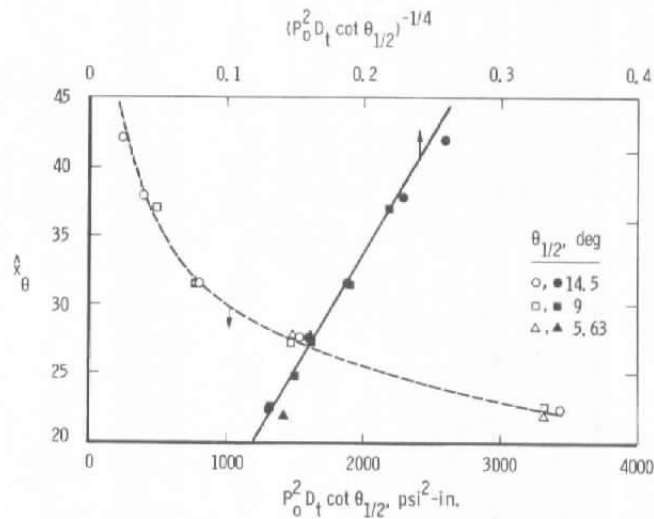


Figure 19. Scaling of conical nozzle condensation onset, N_2 .

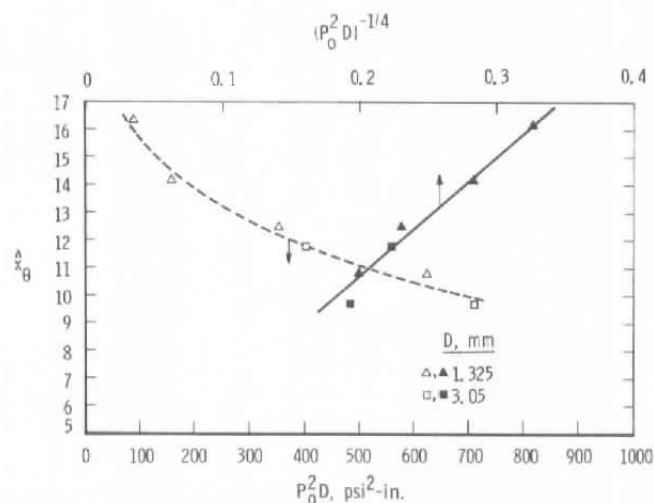


Figure 20. Scaling of sonic orifice condensation onset, N_2 .

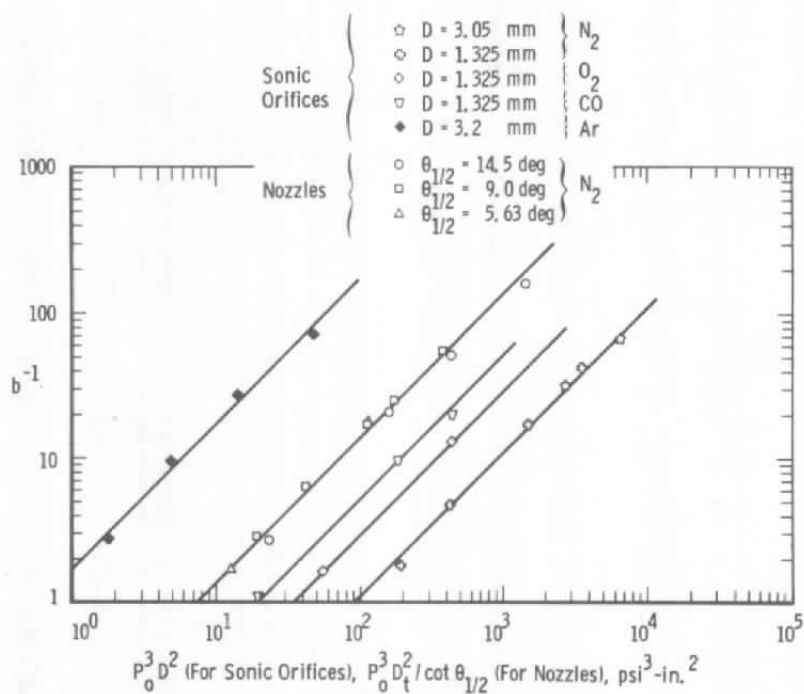


Figure 21. Scattering function scaling.

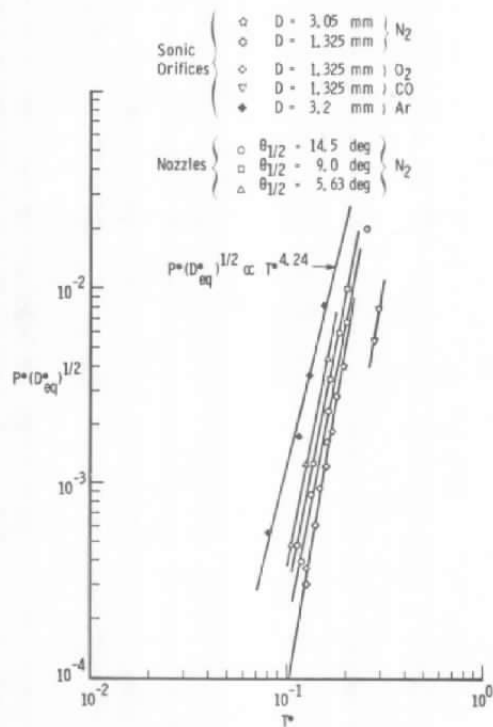


Figure 22. Condensation onset locus using reduced values.

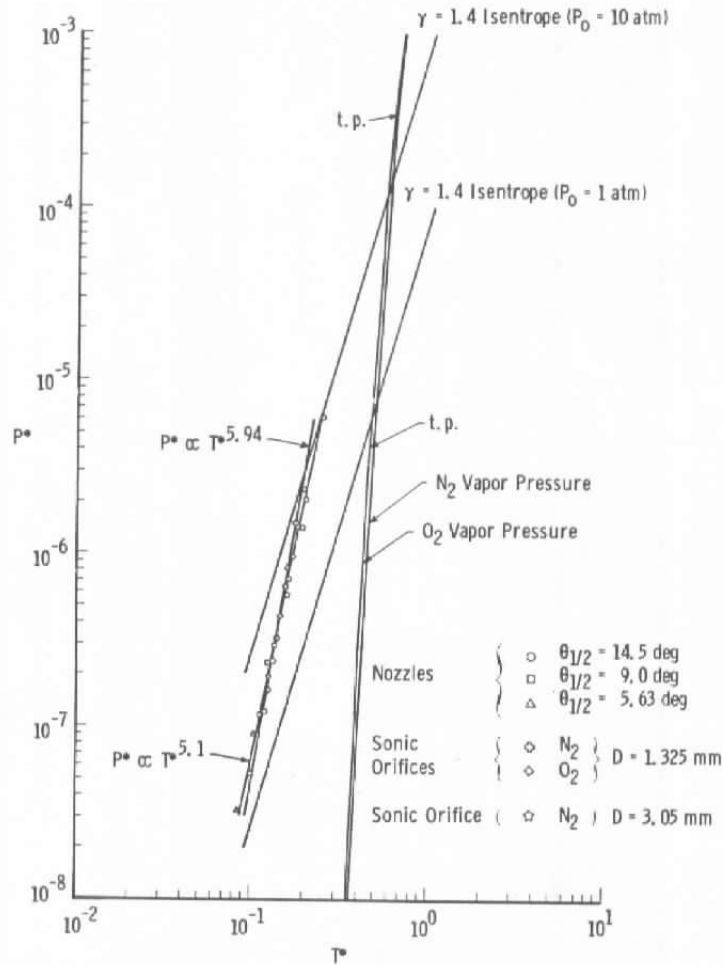


Figure 23. Condensation onset locus using reduced values.

As a check it was desired to derive the form of Eq. (22) for sonic orifices using source flow and isentropic relations and the spatial location of condensation onset relation given by Eq. (12). The source flow relation is

$$\frac{T}{T_0} = c_1(\gamma) \hat{x}^{2-2\gamma} \quad (23)$$

where

$$\left. \begin{aligned} c_1(\gamma = 1.4) &= 0.375 \\ c_1(\gamma = 1.67) &= 0.281 \end{aligned} \right\} \text{Ref. 22.}$$

From the experimental results,

$$\hat{x}_g = c_2 \left[\frac{P_o^2 D}{f_1(T_o)} \right]^{-1/4} \quad (24)$$

where a functional dependence on reservoir temperature, T_o , has been anticipated. The isentropic relation is

$$\frac{P_o}{P} = \left(\frac{T_o}{T} \right)^{\frac{\gamma}{\gamma-1}} \quad (25)$$

For $\gamma = 1.4$, Eqs. (23), (24), and (25) show the condensation onset locus to be of the form

$$P \propto f_2(T_o) T^6 \quad (26)$$

and for $\gamma = 1.67$,

$$P \propto T^{3.99} \quad (27)$$

which compares favorably with Eq. (22) for $\gamma = 1.4$ and with the results shown in Fig. 22 for $\gamma = 1.67$.

For nozzle flow fields the situation is more complex since the source flow relation is no longer valid. A typical T/T_o axial variation is shown in Fig. 24 for the 14.5-deg nozzle. For each of the three values of expansion half-angle, a straight line was fitted to the logarithmic plots of the MOCS-predicted T/T_o axial variation. The results indicated that

$$\hat{x} \propto \left(\frac{T}{T_o} \right)^{-0.928} \quad (28)$$

was a fair approximation for the nozzles. Using Eqs. (28), (14), and (25), the predicted nozzle condensation locus was

$$P \propto f_2(T_o) T^{5.4} \quad (29)$$

which compares favorably with Eq. (21).

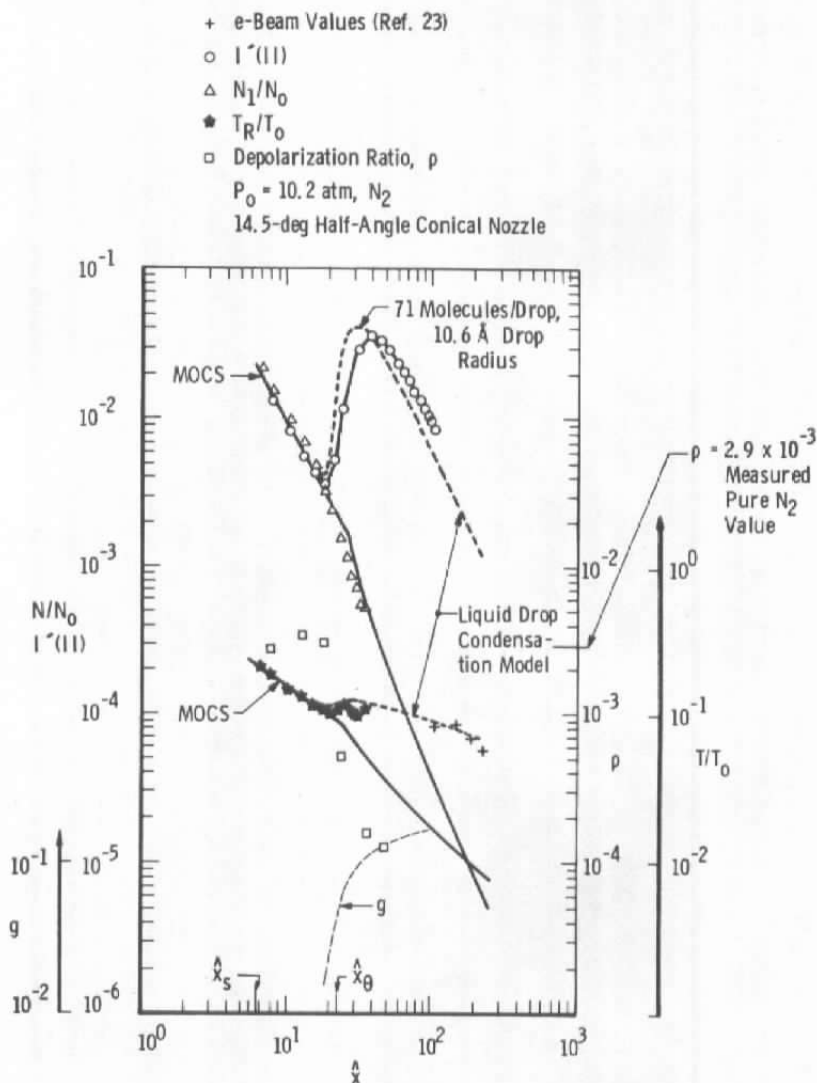


Figure 24. Axial variation of $I^*(II)$, number density, temperature, mass fraction (g), and depolarization ratio: 14.5-deg conical nozzle, $P_0 = 10.2 \text{ atm, N}_2$.

4.3 CORRELATION OF TEMPERATURE, RAYLEIGH SCATTERING, AND DEPOLARIZATION RATIO MEASUREMENTS WITH CONDENSATION

Figures 24 through 30 show the measured axial variation of $I^*(II)$, N/N_0 , and T/T_0 for several P_0 values for N_2 nozzle and sonic orifice flows. The number density and temperatures were obtained using laser-Raman scattering diagnostics (Refs. 13 through 16) and also by

using electron beam fluorescence diagnostics for the specific flow conditions of Fig. 24. It is noted that the monomer number density is little affected by the condensation process; however, the temperature can be increased by as much as 50 percent above the isentropic prediction due to the heat release in the condensation process. It is also observed that the increase in temperature correlates very well with the onset of condensate growth.

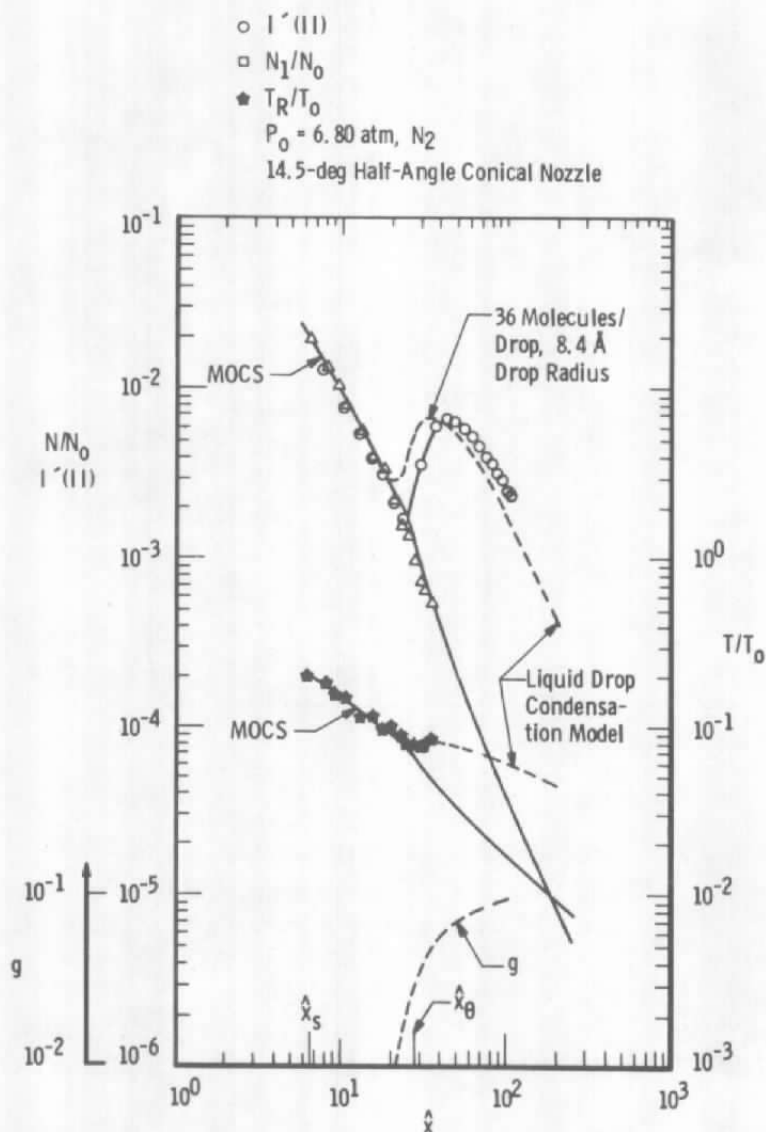


Figure 25. Axial variation of $I'(II)$, number density, temperature, and mass fraction: 14.5-deg conical nozzle, $P_0 = 6.80 \text{ atm, N}_2$.

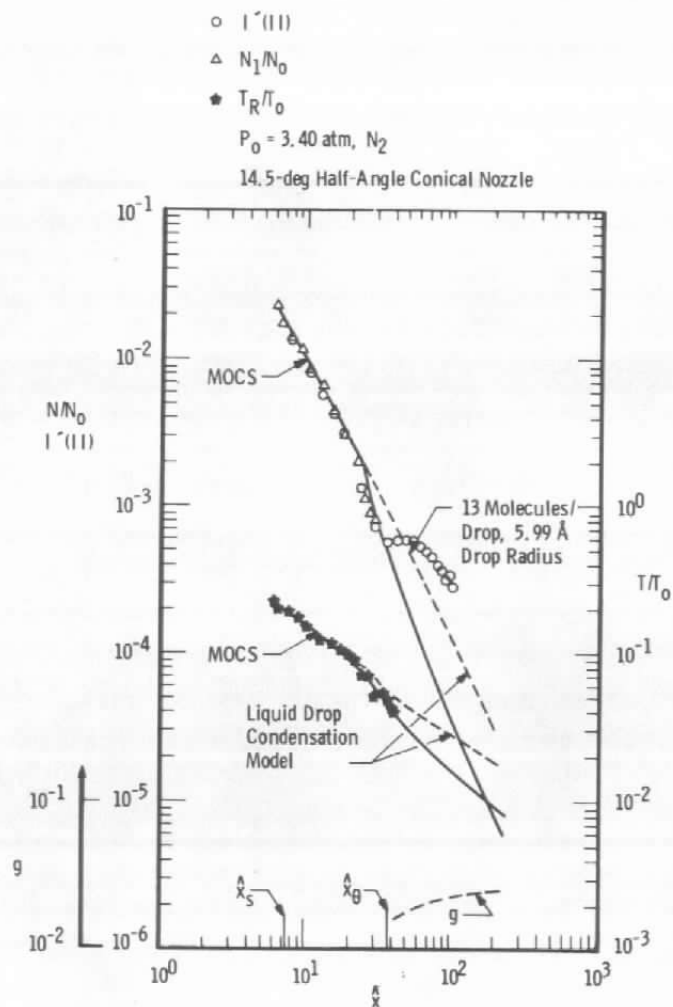


Figure 26. Axial variation of $I'(II)$, number density, temperature, and mass fraction: 14.5-deg nozzle, $P_0 = 3.40 \text{ atm, N}_2$.

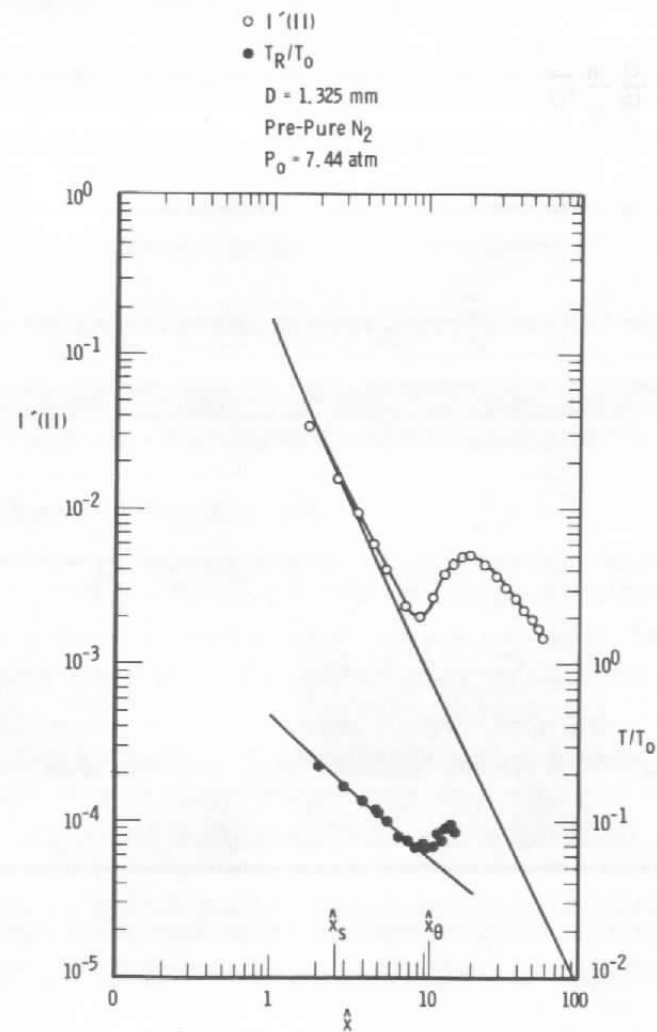


Figure 27. Axial variation of $I'(II)$ and temperature: sonic orifice, $D = 1.325 \text{ mm, } P_0 = 7.44 \text{ atm, atm, N}_2$.

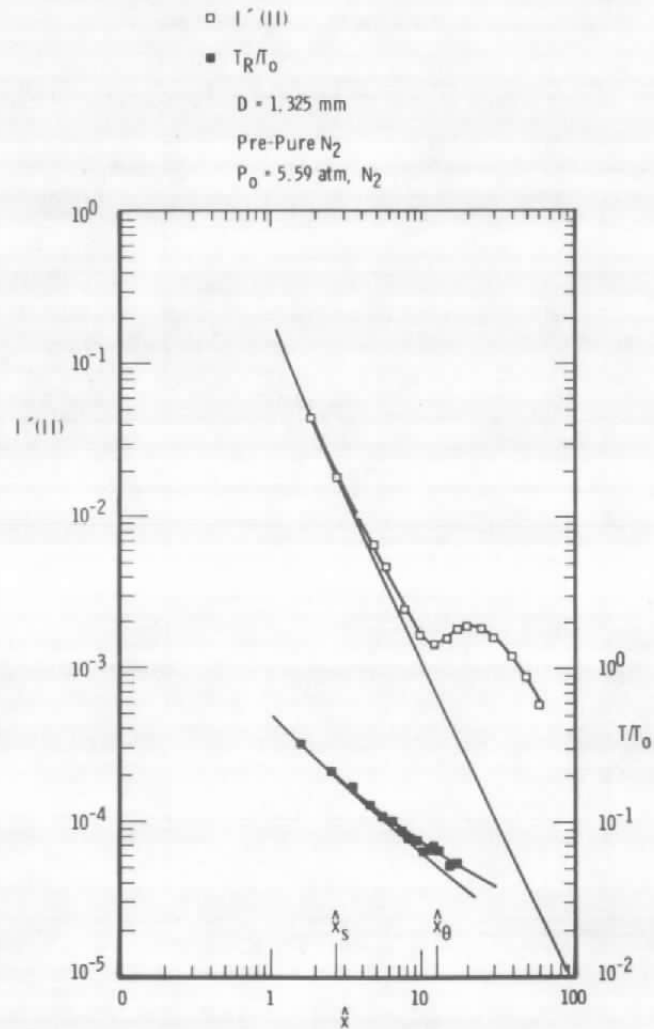


Figure 28. Axial variation of $I'(II)$ and temperature: sonic orifice, $D = 1.325$ mm, $P_0 = 5.59$ atm, N_2 .

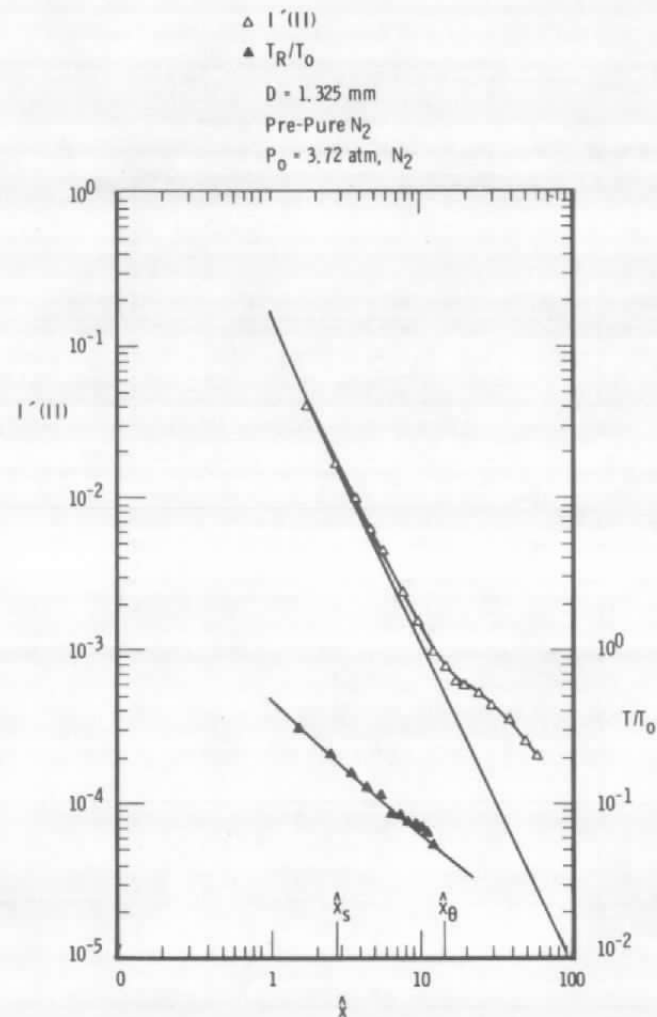


Figure 29. Axial variation of $I'(II)$ and temperature: sonic orifice, $D = 1.325$ mm, $P_0 = 3.72$ atm, N_2 .

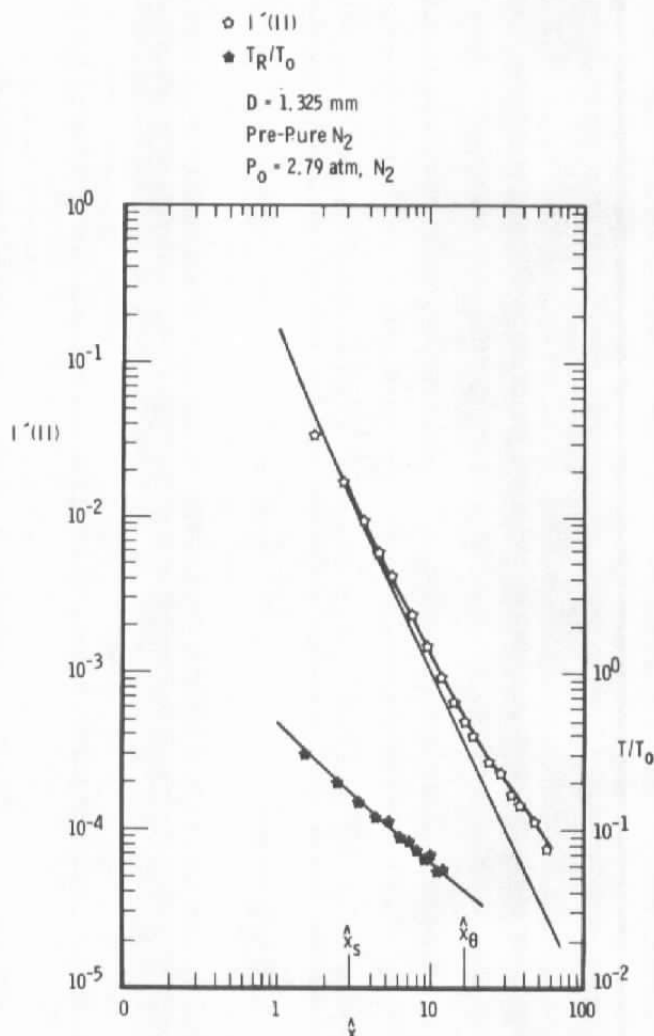


Figure 30. Axial variation of $I'(\text{II})$ and temperature: sonic orifice, $D = 1.325 \text{ mm}$, $P_0 = 2.79 \text{ atm}$, N_2 .

Depolarization measurements of the Rayleigh scattering were performed to acquire some information concerning the asymmetry of the scattering clusters. The axial variation of the depolarization ratio, ρ , for the $P_0 = 10.2 \text{ atm}$, $\theta_{1/2} = 14.5\text{-deg}$ conical nozzle condition is shown in Fig. 24. It is seen that ρ does indeed decrease rapidly from its room temperature monomer value as one proceeds axially through the cluster growth region. This behavior is intuitively expected because as the linear N_2 molecules cluster together they should form more spherical scatterers that contribute a larger portion to the scattered intensity than the monomers. It is interesting

to note that the depolarization ratio axial variation for Ar (Ref. 11) shows an initial rapid increase in ρ followed by a slow decrease. Again this is expected because as the spherical monomeric Ar atoms cluster to form dimers, the depolarization ratio should initially increase; however, with further clustering the depolarization ratio should decrease.

4.4 COMPARISON OF CONDENSATION CALCULATIONS WITH MEASUREMENTS

In order to acquire information regarding condensate mass fraction and cluster size along the centerline of the expansion flow field, a liquid-drop, monodisperse distribution condensation model was used (Refs. 23, 24, and 25). This calculation (developed by M. Kinslow) assumes the condensing flow field to be inviscid, adiabatic, and one-dimensional, with no mass transfer across the streamtube boundary. The gas and condensate are assumed to obey the perfect gas relation. The condensed phase is assumed to be of the form of monodisperse spherical drops or particles which are characterized by bulk properties and to be in the free molecular flow regime relative to the uncondensed phase. Condensate-gas velocity slip effects are ignored; and the condensate growth rate is determined by gas condensate interaction only. The mass accommodation coefficient is assumed to be unity. The initial size and number density of spontaneous nucleation sites were adjustable parameters and were selected to reproduce as closely as possible the experimental results.

The condensation calculation used the flow-field conditions at the saturation point, \hat{x}_g , as the starting data. For the 14.5-deg nozzle, condensation calculations were made for reservoir pressures of 10.2, 6.8, and 3.4 atm, and the results are shown in Figs. 24 through 26, respectively. A mole fraction of 1.33×10^{-3} for dimers was used to obtain the fair agreement between the calculations and measurements. These calculations yield scattering functions within 50 percent of the measured values. The measured axial variations of number density and temperature were obtained using laser-Raman diagnostics (Refs. 13 through 16), and also by using electron beam fluorescence diagnostics for the specific flow conditions of Fig. 24, as previously mentioned. It is seen that the predicted temperature increase due to condensation is in fair agreement with the measured increase.

Also shown in Figs. 24 through 26 is the predicted axial variation of condensate mass fraction, g . For $P_0 = 10.2$ atm, $\hat{x} = 30$, the calculations indicate 71 molecules per drop with a radius of 10.6 \AA . It should be noted that using these molecules/drop values with associated mass fractions, Eq. (5) and the relation $f = J^2 X_J$ give scattering functions an order of magnitude smaller than measured. This indicates that the concept of polarizability additivity is not applicable for clusters this large.

5.0 DISCUSSION AND SUMMARY

With regard to the experimental data and MOCS calculations shown in Figs. 7 through 9 and 24 through 26, it is noted that the MOCS shows a discontinuity in slope for the axial profiles of $I'(\text{II})$ or N/N_0 and T/T_0 . This is due to expansion effects from the nozzle lip. The experimental data shown in Figs. 24 through 26 would indicate that the discontinuity in slope is not realized in practice.

As noted previously mass spectrometric sampling (Refs. 1, 3, and 20) has shown that dimer concentration scales as $P_0^2 D_{eq}$. It has been observed from this investigation that the condensation onset location (more specifically, the condensate growth onset) scales as $(P_0^2 D_{eq})^{-1/4}$. These results imply that the termolecular dimer formation mechanism is the rate-controlling process for condensation in rapidly expanding, low density flow fields. Remembering that bimolecular reactions scale as $P_0 D_{eq}$ (Ref. 3) and assuming the growth of clusters of trimers and larger species to proceed by bimolecular collisions, one would expect the scattering function, f , to scale as $P_0^3 D_{eq}^2$. The sonic orifice results of this investigation show a $P_0^3 D_{eq}^2$ scaling for the scattering function; however, the nozzle results show a $P_0^3 (D_{eq}^2) / \cot \theta_{1/2}$ scaling for the scattering function, which is in disagreement with the equivalent nozzle concept of Ref. 3. Furthermore, the condensation onset results of this investigation indicate that for a given P_0 and T_0 a decrease in $\theta_{1/2}$ with nozzle length remaining the same will result in decreasing \hat{x}_θ , whereas calculations of Sherman and Griffin (Ref. 24) show that a decrease in $\theta_{1/2}$ with nozzle length changing to maintain a constant area ratio will result in an increasing \hat{x}_θ . However, the calculations of Clark (Ref. 26) for constant nozzle length and throat diameter show qualitative agreement with the condensation onset results of this investigation; quantitative agreement is difficult to assess because of the different definitions of condensation

onset. Future scaling studies will be devoted to variation of T_0 , D_t , and $\theta_{1/2}$ with constant area ratio.

With regard to the use of intermolecular parameters for normalization of the condensation onset loci in the P-T plane, it is quite interesting that the homonuclear N_2 and O_2 show a common locus while the monatomic and polar diatomic species show different loci. This result is in agreement with the results of Yealland, et al. (Ref. 2), although Hagena and Obert (Ref. 3) suggest that the method would be restricted to monatomic species. Future investigation of this normalization procedure will involve NO , HCl , NH_3 , and H_2O .

Further development of condensation calculations for flow fields is needed in order to completely predict the scattering efficacy for expansions of a variety of gases throughout the flow field. Although the present model makes a fair prediction of the axial variation of light scattering, it requires adjustment of initial nuclei size and mole fraction to fit experimental data. Furthermore, the assumption of unity accommodation coefficients and constant nuclei mole fraction is doubtful. The classical capillarity theory of condensation can be used to calculate nucleation rates and hence the size and number of "critical nuclei" at any point in the flow field. Shown in Fig. 31 are nucleation rates calculated for three P_0 values for the 14.5-deg nozzle using the classical nucleation theory. It is noted that nucleation has passed through a maximum and rapidly declined prior to observed condensate growth, indicating the sequential nature of condensation processes in rapid expansions, that is, saturation followed by nucleation followed by condensate growth. However, the capillarity theory is not beyond criticism in spite of some of its successes, because the theory is thermodynamic in nature and not kinetic. Furthermore, variation of surface tension values with radius at small nucleus sizes, extremely large supersaturation ratios such as are found in rapidly expanding flows, and statistical mechanical correction factors can all cause great variation in calculated nucleation rates (Ref. 23). An alternate approach has been described by Dorfeld and Hudson (Refs. 27 and 28). Their method is strictly kinetic in nature, and it provides a method for calculating dimer concentration using termolecular rate equations and also accounts for the effective increase in the termolecular collision rate at low temperature due to the presence of loosely bound orbiting pairs (Ref. 27). Condensate growth is calculated using bimolecular collision rates of monomers with rate-limiting species such as dimers (Ref. 28). It is this approach that will be explored for future condensation calculation development.

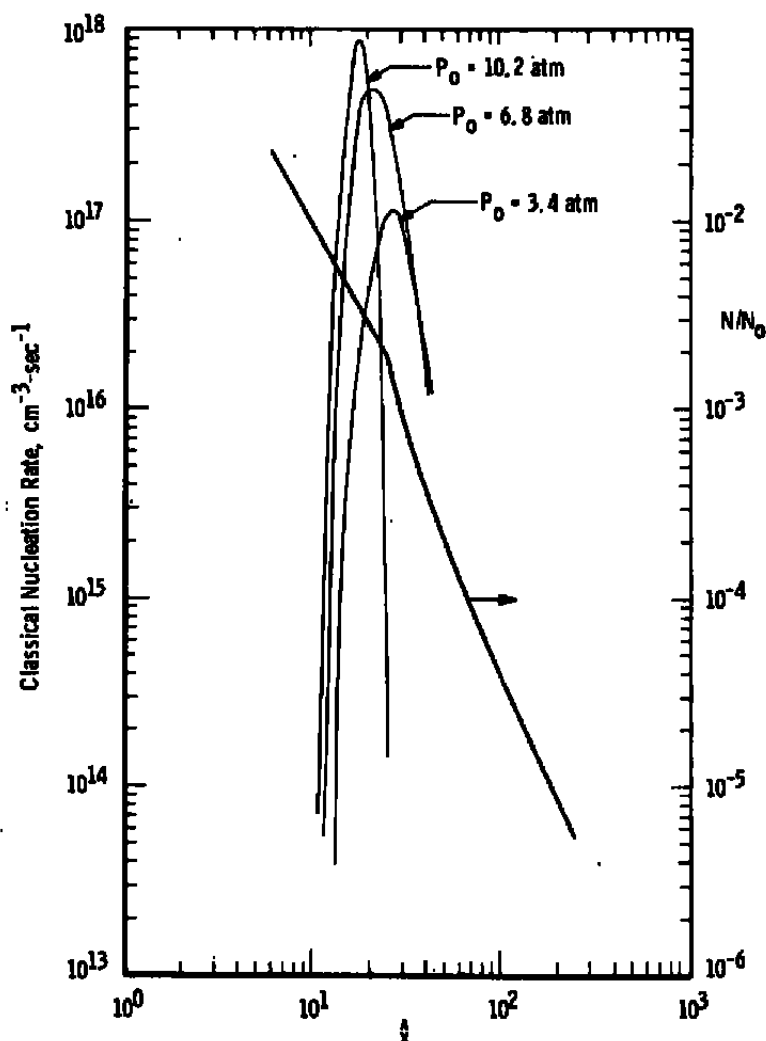


Figure 31. Classical nucleation rates for three N_2 expansions, 14.5-deg conical nozzle.

REFERENCES

1. Golomb, D., Good, R. E., Bailey, A. B., Busby, M. R., and Dawbarn, R. "Dimers, Clusters, and Condensation in Free Jets. II." The Journal of Chemical Physics, Vol. 57, No. 9, November 1972, pp. 3844-3852.
2. Yealland, R. M., Deckers, J. M., Scott, I. D., and Tuori, C. T. "Dimer Concentrations in Supersonic Free Jets." Canadian Journal of Physics, Vol. 50, No. 20, October 15, 1972, pp. 2464-2470.

3. Hagena, O.F. and Obert, W. "Cluster Formation in Expanding Supersonic Jets: Effect of Pressure, Temperature, Nozzle Size, and Test Gas." The Journal of Chemical Physics, Vol. 56, No. 5, March 1972, pp. 1793-1802.
4. Durbin, E. J. "Optical Methods Involving Light Scattering for Measuring Size and Concentration of Condensation Particles in Supercooled Hypersonic Flow." NACA-TN-2441, August 1951.
5. Wegener, P.P. and Stein, G.D. "Light-Scattering Experiments and Theory of Homogeneous Nucleation in Condensing Supersonic Flow." Combustion Institute, International Symposium on Combustion, University of Poitiers, France, 1968, pp. 1183-1190.
6. Stein, G.D. "Angular and Wavelength Dependence from a Cloud of Particles Formed by Homogeneous Nucleation." Dept. of Engineering and Applied Science, Yale University, December 1968.
7. Clumpner, J.A. "Light Scattering from Ethyl Alcohol Droplets Formed by Homogeneous Nucleation." The Journal of Chemical Physics, Vol. 55, No. 10, November 1971, pp. 5042-5045.
8. Beylich, A.E. "Condensation in Carbon Dioxide Jet Plumes." AIAA Journal, Vol. 8, No. 5, May 1970, pp. 965-967.
9. Beylich, A.E. "Experimental Investigation of Carbon Dioxide Jet Plumes." The Physics of Fluids, Vol. 14, No. 5, May 1971, pp. 898-905.
10. Daum, F.L. and Farrell, C.A. "Light Scattering Instrumentation for Detecting Air Condensation in a Hypersonic Wind Tunnel." Fourth International Congress on Instrumentation in Aerospace Simulation Facilities, Brussels, Belgium, June 1971, pp. 209-215.
11. Lewis, J.W.L. and Williams, W.D. "Argon Condensation in Free-Jet Expansions." AE DC-TR-74-32 (AD782445), July 1974.
12. Lewis, J.W.L., Williams, W.D., Price, L.L., and Powell, H.M. "Nitrogen Condensation in a Sonic Orifice Expansion Flow." AE DC-TR-74-36 (AD783254), July 1974.

13. Lewis, J.W.L. and Williams, W.D. "Profile of an Anisentropic Nitrogen Nozzle Expansion." AEDC-TR-74-114 (AD-A004764), February 1975.
14. Williams, W.D. and Lewis, J.W.L. "Raman and Rayleigh Scattering Diagnostics of a Two-Phase Hypersonic N₂ Flowfield." AIAA Journal, Vol. 13, No. 6, June 1975, pp. 709-710.
15. Lewis, J.W.L. and Williams, W.D. "Measurement of Temperature and Number Density in Hypersonic Flow Fields Using Laser Raman Spectroscopy." AIAA Paper No. 75-175, presented at the AIAA 13th Aerospace Sciences Meeting, Pasadena, California, January 20-22, 1975.
16. Williams, W.D. and Lewis, J.W.L. "Rotational Temperature and Number Density Measurements of N₂, O₂, CO, and CO₂ in a Hypersonic Flow Field Using Laser-Raman Spectroscopy." AEDC-TR-75-37 (AD-A012877), July 1975.
17. Prozan, R.J. Lockheed Report No. HREC A782535 (April 1966), available upon request from the Defense Documentation Center, Cameron Station, VA.
18. Ashkenas, H. and Sherman, F.S. Rarefied Gas Dynamics, Fourth Symposium, Vol. II. Edited by J.H. de Leeuw. Academic Press, New York, 1966, pp. 84-105.
19. Hilsenrath, J., Beckett, C.W., Benedict, W.S., Fano, L., Hoge, H.J., Masi, J.F., Nuttal, R.L., Touloukia, Y.S., and Ubbelohde, H.W. Tables of Thermal Properties of Gases. NBS Circular 564, November 1955.
20. Milne, T.A., Vandegrift, A.E., and Greene, F.T. "Mass Spectrometric Observations of Argon Clusters in Nozzle Beams. II. The Kinetics of Dimer Growth." The Journal of Chemical Physics, Vol. 52, No. 3, February 1970, pp. 1552-1560.
21. Hirschfelder, J.O., Curtiss, C.F., and Bird, R.B. Molecular Theory of Gases and Liquids. John Wiley & Sons, New York, 1954.
22. Hagen, O.F. Rarefied Gas Dynamics, Vol. II. Edited by L. Trilling and H.Y. Wachman. Academic Press, New York, 1969, p. 1465.

23. Wegener, P.P. Nonequilibrium Flows, Chapter 4. Part I, Vol. I, of Gasdynamics, edited by P.P. Wegener. Marcel Dekker, New York, 1969, pp. 168-187.
24. Griffin, J.L. and Sherman, P.M. "Computer Analysis of Condensation in Highly Expanded Flows." AIAA Journal, Vol. 3, No. 10, October 1965, pp. 1813-1819.
25. Hill, P.G., Witting, H., and Demetri, E.P. "Condensation of Metal Vapors During Rapid Expansion." Journal of Heat Transfer, Vol. 85, November 1963, pp. 303-317.
26. Clark, D.R. "On the Flow in the Nozzle of a Condensing Diatomic Vapour." CoA R Aero-165, College of Aeronautics, Cranfield, Great Britain.
27. Dorfeld, W.G. and Hudson, J.B. "Condensation in CO₂ Free Jet Expansions. I. Dimer Formation." The Journal of Chemical Physics, Vol. 59, No. 3, August 1973, pp. 1253-1260.
28. Dorfeld, W.G. and Hudson, J.B. "Condensation in CO₂ Free Jet Expansions. II. Growth of Small Clusters." The Journal of Chemical Physics, Vol. 59, No. 3, August 1973, pp. 1261-1265.

NOMENCLATURE

a	Radius of scatterer
a_i	Radius of i-mer
b	A function of reservoir pressure and orifice diameter and expansion half angle
c_0, c_1, c_2, c_3, c_4	Scaling constants
$c(\gamma), c_1(\gamma)$	γ -dependent parameters whose numerical value is given in the text
D	Sonic orifice diameter
D_t	Conical nozzle throat diameter
D_{eq}	Equivalent diameter defined as D for sonic orifices and $c(\gamma) D_t \cot \theta_1/2$ for conical nozzles
D_{eq}^*	D_{eq} normalized by the intermolecular potential parameter σ
f	Rayleigh scattering function defined by Eq. (4)
g	Condensate mass fraction
I	Relative Rayleigh scattering intensity defined by Eq. (1)
$I'(\Pi), I'(I)$	Relative Rayleigh scattering intensity, normalized to the relative Rayleigh scattering intensity of a gas sample of number density N_0 , polarized parallel and perpendicular to the plane of polarization of the incident laser beam, respectively
J	Number of molecules per cluster
K_α	Constant in Eq. (1)
MOCS	Method-of-characteristics solution
N	Number density of gas species
N_i	i-mer number density
N_0	Reservoir number density
N_1^0	Isentropic monomer number density
N_T	Total local number density
n_0, n_1, n_2	Scaling constants

P_O	Reservoir pressure, atm
P_S	Saturation pressure
P_θ	Pressure at condensation onset
$P_{v\theta}$	Equilibrium vapor at condensation onset
P^*	P_θ normalized by the intermolecular potential parameter ϵ/σ^3
r	Radial distance from flow-field centerline
$(s_\theta)^0$	Isentropic supersaturation ratio
$(s_\theta^*)^0$	Isentropic degrees of supercooling
T_O	Reservoir temperature, K
T_S	Saturation temperature
T_θ	Temperature at condensation onset
T^*	T_θ normalized by the intermolecular potential parameter ϵ/k
t. p.	Thermodynamic triple point
X_i	i-mer mole fraction
\hat{x}	Axial position in flowfield, $\hat{x} = x/D$ for sonic orifices and $\hat{x} = x_t/D_t$ for conical nozzles
\hat{x}_S	Axial location of saturation
\hat{x}_θ	Axial location of condensation onset
α	Polarizability
α_i	i-mer polarizability
γ	Specific heat ratio
$\epsilon/k, \epsilon/\sigma^3$	Intermolecular potential parameters given in Table 4
$\theta_{1/2}$	Expansion half-angle of conical nozzle
λ	Wavelength of scattered radiation
ρ	Depolarization ratio of Rayleigh scattering
σ	Intermolecular potential parameter given in Table 4